Modelling the archaeomagnetic field under spatial constraints from dynamo simulations: a resolution analysis

Sébastien Sanchez, A. Fournier, J. Aubert, E. Cosme, Y. Gallet

Geophysical Journal International

Geophys. J. Int. (2016) **207,** 983–1002
Advance Access publication 2016 August 24
GJI Geomagnetism, rock magnetism and palaeomagnetism

doi: 10.1093/gji/ggw316

Modelling the archaeomagnetic field under spatial constraints from dynamo simulations: a resolution analysis

S. Sanchez,[1] A. Fournier,[1] J. Aubert,[1] E. Cosme[2] and Y. Gallet[1]

[1] *Institut de Physique du Globe de Paris, Sorbonne Paris Cité, Université Paris Diderot, CNRS (UMR 7154), Paris, France. E-mail: ssanchez@ipgp.fr*
[2] *Université Grenoble Alpes-CNRS, LGGE, Grenoble, France*

Accepted 2016 August 19. Received 2016 August 7; in original form 2016 March 4

SUMMARY

Archaeomagnetic observations are key to recovering the behaviour of the geomagnetic field over the past few millennia. The corresponding data set presents a highly heterogeneous distribution in both space and time. Furthermore, the data are affected by substantial age and experimental uncertainties. In order to mitigate these detrimental properties, time-dependent global archaeomagnetic field models are usually constructed under spatial and temporal regularization constraints, with the use of bootstrap techniques to account for data uncertainties. The models so obtained are the product of an adjustable trade-off between goodness-of-fit and model complexity. The spatial complexity is penalized by means of a norm reflecting the minimization of Ohmic dissipation within the core. We propose in this study to resort to alternative spatial constraints relying on the statistics of a numerical dynamo simulation with Earth-like features. To that end, we introduce a *dynamo norm* in an ensemble least-squares iterative framework, the goal of which is to produce single-epoch models of the archaeomagnetic field. We first validate this approach using synthetic data. We next construct a redistributed archaeomagnetic data set between 1200 BC and 2000 AD by binning the data in windows of 40-yr width. Since the dynamo norm is not adjustable, we can legitimately calculate a resolution matrix to quantify the resolving power of the available archaeomagnetic data set. Gauss coefficients are resolved up to spherical harmonic degree 3 for the first thousand years of the interval, to degree 4 for the next thousand years and to degree 5 during the last millennium. These conclusions are based on the distribution and uncertainties that characterize the data set, and do not take into account the possible presence of outliers. Comparison between our model, called AmR, and previously published archaeomagnetic field models confirms the archaeomagnetic resolution analysis: it highlights the dichotomy between data-driven coefficients for which model predictions coincide (within their respective uncertainties), and prior-driven coefficients. This study opens the way to physics-based models of the archaeomagnetic field; future work will be devoted to integrating the framework here introduced into a time-dependent ensemble assimilation scheme.

Key words: Inverse theory; Archaeomagnetism; Dynamo: theories and simulations.

1 INTRODUCTION

The main source of the Earth's magnetic field is located in the Earth's core. Composed mainly of iron, the core is in liquid phase in its external part and solid in its interior. The temperature gradient between the inner and outer boundaries, together with the release of lighter buoyant elements from the crystallization of the inner core, induces convection within the outer core. Such convective motions of the highly conductive iron flow enable electromagnetic induction, generating a magnetic field via a dynamo process. This process, affected by the Coriolis force due to the Earth's rotation, produces a mainly dipolar structure of the global magnetic field, roughly aligned with the rotation axis. There are, however, important departures from dipolarity, like the presently observed South Atlantic Magnetic Anomaly. The westward drift and spread of this anomaly, as well as the intensity decrease of the axial dipole throughout the past hundred years, are important aspects of the latest secular variation (SV) of the Earth's magnetic field (Jackson *et al.* 2000; Hartmann & Pacca 2009; Finlay *et al.* 2010).

Although current direct measurements of the magnetic field offer global coverage in terms of very precise satellite, magnetic observatory and survey data, the magnetic field and its SV beyond the past few centuries remain far less constrained. The key to unravel it relies on the indirect magnetic field information provided by the

remanent magnetization acquired by geological deposits (mainly lava flows) and archaeological artefacts at the time of their formation, emplacement, fabrication or use. These observations are known as archaeomagnetic data, which are compiled in global databases, such as GEOMAGIA (Donadini *et al.* 2006; Brown *et al.* 2015), for directional and intensity data covering the past 50 millennia, and ArcheoInt (Genevey *et al.* 2008) for intensity data over the past 10 millennia. Unfortunately, these data sets are clustered around some specific areas of the globe, like Europe and western Asia, leaving the South Hemisphere practically undocumented. They are also sparse before the last two thousand years. However, it is important to note that a significant effort has been made by the archaeomagnetism community into improving the databases, not only by extending the data catalogue, but also by recalibrating age uncertainty estimates. For instance, new data from South America, Africa and Oceania were recently incorporated into the third and newer version of GEOMAGIA (Brown *et al.* 2015), slightly decreasing the biasing of observations towards the North Hemisphere. Still, despite their challenging character, archaeomagnetic compilations have allowed the development of several inverse models of the global magnetic field spanning the past few millennia (Hongre et al. 1998; Korte & Constable 2005; Korte *et al.* 2011; Licht *et al.* 2013; Nilsson *et al.* 2014; Pavón-Carrasco *et al.* 2014).

Inverse magnetic field models are the result of a minimization of the misfit between data and model, generally regularized in space and time by a certain norm of the model to restrict the solution of such an ill-posed inverse problem (Gubbins & Bloxham 1985). The regularization is based on prior information built on the hypothesis that the core magnetic field varies smoothly in time and that the dissipation of magnetic energy at the core–mantle boundary (CMB) is minimum (Gubbins 1975; Bloxham & Jackson 1992). The shorter temporal and spatial scales of inverse geomagnetic field models are consequently damped, thereby concealing a possibly more complex behaviour of the geomagnetic field. As an alternative, different constraints can be sought in numerical simulations of the Earth's dynamo, which make it possible to understand the main dependencies between the field variables of the dynamo system and also to construct, for instance, the statistics describing the variability of the magnetic field at the CMB. Such statistics can be used to define a 'dynamo norm' to constrain the archaeomagnetic inverse problem, in place of the canonical regularizations discussed above. We shall explore this possibility in this study.

Different kinds of dynamo models can be built depending on the control parameters and coupling mechanisms within the different regions of the deep Earth. Some standard dynamo models, considering thermochemical convection as the driving mechanism of the system, succeed in displaying an Earth-like morphology of the magnetic field relative to reference inverse models (Christensen *et al.* 2010), but fail to present an Earth-like SV pattern (see for instance the standard model of Aubert *et al.* 2013). However, another model designed by Aubert *et al.* (2013) is able to reproduce the localized westward drift of low latitude magnetic anomalies, like the South Atlantic Anomaly. The model, coined 'Coupled Earth', considers gravitational coupling mechanisms and heterogeneous crystallization of the inner core to produce an Earth-like SV. Given its Earth-likeness, the statistical information from Coupled Earth can be used as prior information in the problem of estimating the magnetic field at the CMB (e.g. Aubert 2014).

Estimating the state of a system given a set of noisy observations together with a prior model state is a filtering problem (Jazwinski 1970), for which Kalman filter-based algorithms are largely used. However, while errors are usually prescribed for observations, uncertainties affecting the prior information are difficult to assess. An option is to work with an ensemble of numerical simulations, a strategy at the heart of the Ensemble Kalman filter (EnKF; Evensen 2003). In this case, the prior estimate is given by the mean of an ensemble of model states derived from the numerical integration of the system in question, while prior uncertainties are represented by the sample ensemble covariance. Assuming the ensemble covariance is a good proxy for model error, the EnKF will update the prior information in light of the observations and produce a posterior estimate (also called the analysis), characterized by its mean and covariance.

The EnKF is one example of the many techniques used in the data assimilation framework, the backbone of which relies on a dynamical model describing the physics of a system to be updated with information from its observations. Although data assimilation has been widely used in meteorology and oceanography (Kalnay 2003), it has begun to be explored in geophysics only recently. In particular, an introduction to data assimilation applied to the specific problematic of the Earth's magnetic field can be found in Fournier *et al.* (2010). So far, the ongoing work on geomagnetic data assimilation has focused on updating a numerical model of the geodynamo with Gauss coefficients of the magnetic field as input data (e.g. Fournier *et al.* 2013; Li *et al.* 2014; Tangborn & Kuang 2015). Although the results are promising, in terms of propagation of information from the CMB throughout the core (see also Kuang *et al.* 2009; Aubert & Fournier 2011, for earlier attempts), in an ideal data assimilation scenario raw pointwise observations of the magnetic field should be assimilated in place of field model coefficients.

We present in this paper a preliminary attempt at assimilating such pointwise observations, whose goal is to model the archaeomagnetic field at a given time, under the spatial constraint specified by the Coupled Earth dynamo norm. For simplicity, we ignore at this stage the possibility of performing a temporal sequence of analyses (as permitted by a full EnKF setup), and focus instead on the impact of the dynamo norm on single-epoch field models. In order to ease comparison of our temporally unregularized approach with previously published archaeomagnetic field models for the period 1200 BC to 2000 AD, we resort to the Geomagia50.V2 database of Donadini *et al.* (2006, 2009) that was used to produce these models (in place of the more recent update of GEOMAGIA by Brown *et al.* 2015).

This paper can be summarized as follows. We begin by presenting the estimation method and the dynamo model in Section 2, including details of the archaeomagnetic observation operators, the ensemble approach and a synthetic validation test. Next, in Section 3 we apply the methodology to an archaeomagnetic context, focusing on the resolving power of archaeomagnetic data. Section 4 describes a dynamo-based archaeomagnetic field model relying on a archaeomagnetic data set redistributed over time to take into account age uncertainties, which we compare with previously published models. A summary and some perspectives are finally given in Section 5.

2 METHOD AND MODEL

2.1 Generalized least-squares iterative framework

At any given epoch, we wish to minimize a functional $\mathcal{J}$ of the form

$$\mathcal{J}(\mathbf{x}) = [\mathbf{y} - \mathcal{H}(\mathbf{x})]^T \mathbf{R}^{-1} [\mathbf{y} - \mathcal{H}(\mathbf{x})] + (\mathbf{x} - \mathbf{x}^b)^T \mathbf{P}^{b^{-1}} (\mathbf{x} - \mathbf{x}^b) \quad (1)$$

in which the observations $\mathbf{y}$, whose error covariance matrix is denoted by $\mathbf{R}$, are nonlinearly connected with the system state $\mathbf{x}$, by means of a nonlinear observation operator $\mathcal{H}$. The initial guess on the state, $\mathbf{x}^b$, also called the background, is characterized by the background error covariance matrix $\mathbf{P}^b$. Unless otherwise noted, all vectors are column vectors, and superscript T denotes transposition.

The solution to this problem is sought iteratively, by constructing a sequence of $\mathbf{x}^k$ such that (Tarantola & Valette 1982, eq. 23)

$$\mathbf{x}^{k+1} = \mathbf{x}^b + \mathbf{P}^b\mathbf{H}^{k\,T}(\mathbf{H}^k\mathbf{P}^b\mathbf{H}^{k\,T} + \mathbf{R})^{-1} \times \left[\mathbf{y} - \mathcal{H}\left(\mathbf{x}^k\right) + \mathbf{H}^k\left(\mathbf{x}^k - \mathbf{x}^b\right)\right] \tag{2}$$

or, equivalently (Tarantola & Valette 1982, eq. 25),

$$\mathbf{x}^{k+1} = \mathbf{x}^k + (\mathbf{H}^{k\,T}\mathbf{R}^{-1}\mathbf{H}^k + \mathbf{P}^{b\,-1})^{-1} \times \left\{\mathbf{H}^{k\,T}\mathbf{R}^{-1}\left[\mathbf{y} - \mathcal{H}\left(\mathbf{x}^k\right)\right] - \mathbf{P}^{b\,-1}\left(\mathbf{x}^k - \mathbf{x}^b\right)\right\}, \tag{3}$$

starting in both cases with the initial guess $\mathbf{x}^0 = \mathbf{x}^b$. In these equations, $\mathbf{H}^k$ refers to the observation operator linearized about the current estimate,

$$\mathbf{H}^k = \left.\frac{\partial\mathcal{H}}{\partial\mathbf{x}}\right|_{\mathbf{x}=\mathbf{x}^k}. \tag{4}$$

These two formulations of the iterative algorithm assume that data and background errors are independent. They are equivalent mathematically, but their effective cost differs, depending on the respective size of the data and state vectors, $n_\mathbf{y}$ and $n_\mathbf{x}$, respectively. eq. (3) should be preferred in situations where $n_\mathbf{y} \gg n_\mathbf{x}$, as is the case for standard geomagnetic inverse problems where the model is truncated to low dimensions (e.g. Jackson *et al.* 2000; Korte *et al.* 2009). Eq. (2) is, however, more expedient if $n_\mathbf{y} \ll n_\mathbf{x}$. As will be clear in Sections 2.3 and 3.1, the state and observation vectors dimension considered here correspond to the latter situation. We therefore choose the algorithm defined by eq. (2), for which, once convergence is reached, the uncertainty affecting the final estimate $\hat{\mathbf{x}}$ is given by the posterior covariance matrix

$$\hat{\mathbf{P}} = [\mathbf{I} - \mathbf{P}^b\hat{\mathbf{H}}^T(\hat{\mathbf{H}}\mathbf{P}^b\hat{\mathbf{H}}^T + \mathbf{R})^{-1}\hat{\mathbf{H}}]\mathbf{P}^b, \tag{5}$$

where $\mathbf{I}$ is the identity matrix, and we understand that $\hat{\mathbf{H}}$ denotes the observation operator linearized about the final estimate of the state, $\hat{\mathbf{x}}$. The resolution matrix $\hat{\mathbf{S}}$, which relates to how well the final estimate $\hat{\mathbf{x}}$ resolves the true model state $\mathbf{x}^t$ given the observations, is defined as

$$\hat{\mathbf{S}} = \mathbf{P}^b\hat{\mathbf{H}}^T(\hat{\mathbf{H}}\mathbf{P}^b\hat{\mathbf{H}}^T + \mathbf{R})^{-1}\hat{\mathbf{H}}. \tag{6}$$

In this nonlinear context, the interpretation of $\hat{\mathbf{S}}$ is subject to caution, as high-order derivatives of $\mathcal{H}$ are neglected in the analysis, in the hope that the final estimate is close to the true state. We will check on the validity of this assumption when dealing with synthetic data, in Section 2.6 below.

In standard geomagnetic field modelling, the prior information can be used to motivate regularization constraints on the sought solution, by setting

$$\mathbf{P}^b = \lambda^{-1}\mathbf{C}, \tag{7}$$

where λ is an adjustable 'damping' parameter and $\mathbf{C}$ a suitably chosen matrix, see for example, Bloxham *et al.* (1989), eqs (3.8)–(3.11). The novelty of our approach stands in the prior information we supply, which rests on the statistics of a numerical dynamo simulation, a dynamo norm, and in the ensemble approach that we adopt in order to assess the uncertainties of our estimate of the archaeomagnetic field. We dedicate the next paragraphs to these aspects. We begin by the description of the numerical simulation, the choice of which in turn dictates the nature of the state vector $\mathbf{x}$.

2.2 A geodynamo model as source of prior information

The essential physics of the dynamo can be explained by the interaction between the fluid flow, magnetic field, temperature and composition within the core. Such interactions are governed by the magnetohydrodynamic (MHD) equations, which for the case of the Earth's core are often considered in the Boussinesq approximation due to the weak density stratification of the outer core (e.g. Braginsky & Roberts 1995). Given the complexity of the dynamo system, the MHD dynamo equations are solved by a numerical approximation in a rotating spherical shell (consult Christensen & Wicht 2015, for a recent review on numerical dynamo simulations). The parameter space reached by numerical simulations is, however, restricted by computational feasibility, resting still far away from Earth-like values (Glatzmaier 2002; Christensen & Wicht 2015). This distance in parameters together with uncertainties regarding boundary conditions stresses the imperfect character of the dynamo simulations in representing the geodynamo. Despite this likely misrepresentation, many numerical simulations have been claimed to be Earth-like. To address the issue of semblance between simulations and the magnetic field of the Earth, Christensen *et al.* (2010) defined several morphological criteria to characterize the Earth-likeness of the output of numerical dynamo simulations. However, such criteria aim at describing only the static, morphological semblance with the recent configurations of the Earth's magnetic field, leaving aside its dynamical aspect.

2.2.1 The Coupled Earth dynamo model

Although archaeomagnetic field features have been shown to drift both to the west and the east at high latitudes, a systematic westward drift is observed around the equator, especially in the Atlantic hemisphere, most notably in historical data (Finlay & Jackson 2003; Dumberry & Finlay 2007). Such geographical concentration of the SV strongly suggests a persistent heterogeneous control from the upper and/or lower boundaries of the core. Furthermore, the evidence for seismic anisotropy at the top of the inner core (e.g. Souriau & Calvet 2015, for a review) may indicate a hemispherical dichotomy in terms of inner core growth and therefore of buoyancy release at the inner core boundary (ICB; Alboussière *et al.* 2010; Monnereau *et al.* 2010). In light of these studies, Aubert *et al.* (2013) proposed a bottom-up control of the dynamo by the inner core. Their 'Coupled Earth' model considers a heterogeneous buoyancy control at the ICB, which when combined with the heterogeneous heat-flux control at the CMB is responsible for a higher SV underneath the Atlantic hemisphere. Moreover, the model also includes the gravitational interaction of the lower mantle mass anomalies with the inner core, which results in large scale westward flow (and concurrent advection of field structures) beneath the CMB at low latitudes. The 'Coupled-Earth' model is referred to as CE henceforth.

In this study, we aim at investigating the influence of the statistical properties of a dynamo simulation, the CE model, on the estimation of the magnetic field at the CMB. To that end, we need to find the correspondence between the magnetic field strength and its time scales from the numerical simulation (which operates in a non-dimensional world) and those observed. As in Aubert *et al.* (2013), dimensional rescaling of time in the CE dynamo is performed by calculating the model non-dimensional secular variation

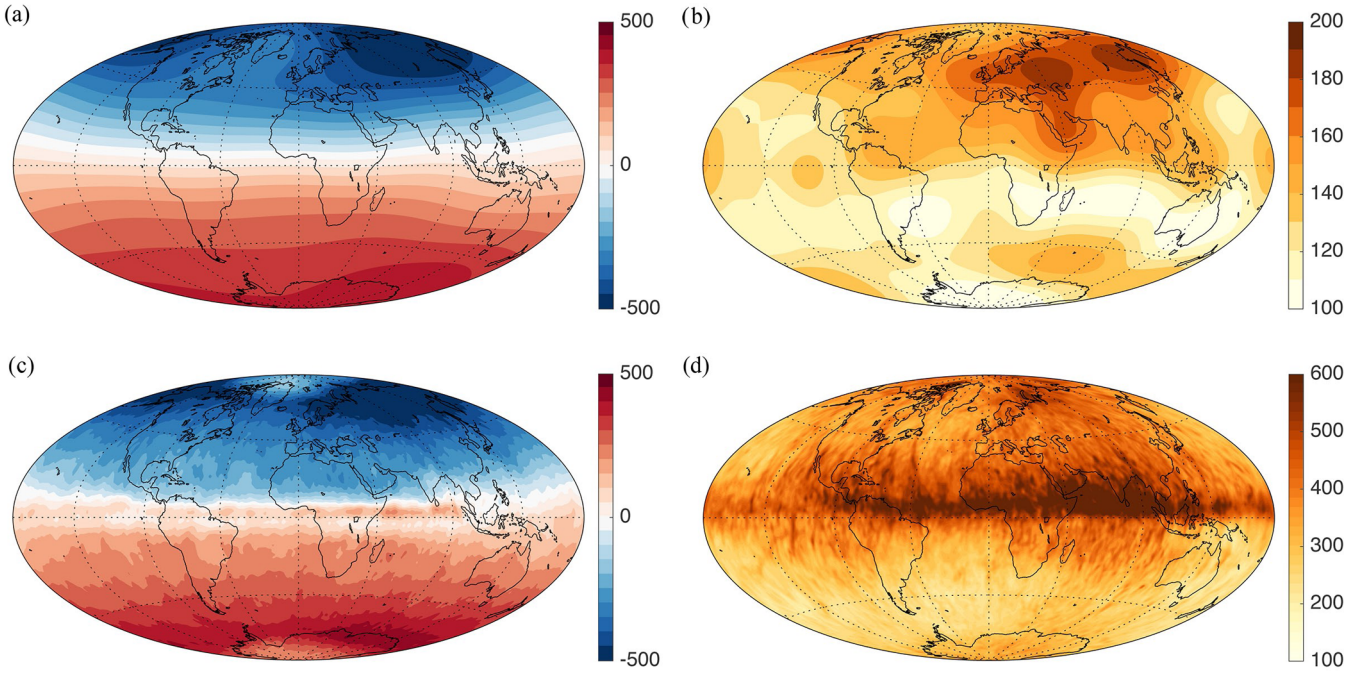

Figure 1. Mean and spread of the radial magnetic field at the CMB of the Coupled Earth (CE) dynamo model. (a) and (b) are respectively the mean and spread truncated at spherical harmonic degree $L = 5$, with contours every 50 μT; (c) and (d) are the mean and spread at the native model truncation, $L = 133$, with contours every 10 μT. All values in μT.

time-scale τ_m and normalizing it to the Earth's SV estimate for the last decade based on satellite data, $\tau_\oplus \approx 415$ yr (Lhuillier *et al.* 2011). The rescaling ratio $\tau_\oplus/\tau_m$ is found to be 56113 yr. The magnetic field, on the other hand, is calibrated here by adjusting the non-dimensional root-mean-squared axial dipole over a 3000 yr interval of the CE simulation, B_m, to that of the 3000 yr root-mean-squared archaeomagnetic model A_FM-0 of Licht *et al.* (2013), $B_\oplus$, giving a magnetic field rescaling ratio $B_\oplus/B_m$ of 850.6 μT. It is important to note that once the calibration is so defined, it leaves no room for an additional adjustable parameter factorizing the dynamo norm $\mathbf{P}^b$ entering the estimation problem (eq. 1).

2.2.2 *Statistical properties of the Coupled Earth dynamo model*

After rescaling the CE dynamo simulation, we define two basic statistical characteristics of the numerical simulation, namely the mean and spread (covariance) of the radial magnetic field B_r at the CMB. Instead of considering the whole simulation interval, we define an ensemble of 820 states of the radial magnetic field at the CMB by randomly picking snapshots on a long sequence of the dynamo simulation, over an interval of about 100 000 yr (the value of 820 ensures statistical convergence of the model state variables). The mean and spread of this ensemble projected in physical space are shown in Fig. 1 for two spherical harmonic (SH) truncations (5 and 133, the latter being that of the native CE model). The average CE model shows an eccentric axial dipole, concentrated underneath northern Asia. Such a feature corresponds to the heterogeneous forcing from the inner boundary (Olson & Deguen 2012) and is in agreement with recent configurations of the magnetic field. However, as Olson & Deguen (2012) pointed out, the eccentric dipole registered from archaeo/palaeomagnetic field models for the last 10 000 yr (Korte & Constable 2011; Korte *et al.* 2011) shows a tendency towards the western hemisphere, while models for older periods show the opposite trend (Johnson & Constable 1997). It is important to bear in mind that although strong hypothesis on the driving mechanism for the dipole eccentricity have been proposed (Olson & Deguen 2012), the resolution of archaeo/palaeomagnetic field models is limited given the sparse data set, possibly compromising a robust assessment of the long term eccentric dipole characteristics (Finlay 2012).

The eccentric dipole from CE discussed above is shown not to be sensitive to the truncation level, as seen by the similarity between Figs 1(a) and (c) despite the different truncations. In contrast, the spread varies with the truncation, in morphology and intensity. As shown by Figs 1(b) and (d), it is mostly concentrated underneath the Earth's northeast quadrant for the larger scales, and around low latitudes between 90°W and 90°E for the smaller scales. The biased distribution of the spread illustrates the effect of the combination of heterogeneous thermal-chemical couplings at the ICB and CMB. These two pieces of information, the mean and covariance of the radial magnetic field at the CMB, define the prior information that fuels the iterative procedure outlined in Section 2.1.

2.3 The state vector x

Due to its solenoidal nature, the magnetic field vector $\mathbf{B}$ can be described in terms of its poloidal and toroidal components $\mathbf{B}_\mathcal{P}$ and $\mathbf{B}_\mathcal{T}$,

$$\begin{aligned}\mathbf{B}(r,\theta,\phi) &= \mathbf{B}_\mathcal{P}(r,\theta,\phi) + \mathbf{B}_\mathcal{T}(r,\theta,\phi)\\ &= \nabla\times\nabla\times[\mathcal{P}(r,\theta,\phi)\mathbf{r}] + \nabla\times[\mathcal{T}(r,\theta,\phi)\mathbf{r}]\,, \qquad (8)\end{aligned}$$

where $\mathcal{P}$ and $\mathcal{T}$ are the poloidal and toroidal scalars and $\mathbf{r}$ is the radius vector (e.g. Dormy 1997). This decomposition is used in the CE model, in which the poloidal and toroidal scalars are further projected onto an SH basis to account for their horizontal dependency. The poloidal scalar at a given radius r is expressed as

$$\mathcal{P}(r,\theta,\phi) = \sum_{\ell=1}^{L}\sum_{m=-\ell}^{\ell}\mathcal{P}_\ell^m(r)Y_\ell^m(\theta,\phi), \qquad (9)$$

where $Y_\ell^m = e^{im\phi} P_\ell^m(\cos\theta)$ is a complex-valued, fully normalized SH of degree ℓ and order m, and L is the truncation of the expansion. As the toroidal field does not have a radial component, it is confined within the core (under the assumption that the mantle is an electrical insulator). For that reason, the only observable part of the core field at the Earth's surface is the poloidal field. We consequently define the (column) state vector of our system by

$$\mathbf{x} \equiv \left[\ldots, \mathcal{P}_\ell^m(r_c), \ldots\right]^T, \tag{10}$$

that is, the poloidal scalar in spectral space at the CMB (radius $r_c = 3485$ km), which is a native component of the state vector characterizing the full CE simulation, for all admissible values of degree ℓ and order m below the truncation of degree and order $L = 133$ ($n_\mathbf{x} = 9045$). We use the full CE truncation bearing in mind the future application of the present methodology to sequential archaeomagnetic assimilation, a situation in which the full set of dynamo state variables define the model state vector.

As stated above, our state vector rests on a fully normalized, complex-valued SH basis. Consequently, in order to connect its components with the standard Gauss coefficients g and h (whose definition rests on the use of real-valued SHs subject to the Schmidt convention for normalization), one must resort to the following relationships

$$g_\ell^m = \left(\frac{r_c}{r_a}\right)^{\ell+2} \frac{\ell\sqrt{2\ell+1}}{r_c} \mathrm{Re}\left[\mathcal{P}_\ell^m(r_c)\right], \tag{11}$$

$$h_\ell^m = -\left(\frac{r_c}{r_a}\right)^{\ell+2} \frac{\ell\sqrt{2\ell+1}}{r_c} \mathrm{Im}\left[\mathcal{P}_\ell^m(r_c)\right], \tag{12}$$

in which Re[] and Im[] denote the real and imaginary parts, and r_a is the mean radius of the Earth ($r_a = 6371.2$ km). If $\mathbf{g}$ represents the vector of Gauss coefficients, one can introduce a matrix $\mathbf{Q}$ to represent the above formula

$$\mathbf{g} = \mathbf{Q}\mathbf{x}. \tag{13}$$

2.4 The observation operator $\mathcal{H}$

As introduced above, the observation operator $\mathcal{H}$ connects the state $\mathbf{x}$ we just defined mathematically with the observations of the magnetic field, $\mathbf{y}$.

The full magnetic field vector observed at the surface of the Earth is described today by its X (north), Y (east) and Z (downward) components. Under the assumption of an insulating mantle, each component can be expressed as a linear functional of the magnetic field B_r at the CMB, by means of a convolution with the adequate Green function for the exterior Laplace problem (Gubbins & Roberts 1983). For example, a measurement of Z at a location (r_0, θ_0, ϕ_0) at Earth's surface writes

$$Z(r_0, \theta_0, \phi_0) = \int_S G_Z(r_0, \theta_0, \phi_0 | r_c, \theta, \phi) B_r(r_c, \theta, \phi) \mathrm{d}S, \tag{14}$$

where G_Z is the Green function (or data kernel) for a Z datum (e.g. Bloxham *et al.* 1989; Constable *et al.* 1993) and S is the core surface of radius r_c. Using SHs, B_r at the core surface is expressed as

$$B_r(r_c, \theta, \phi) = \sum_{\ell=1}^{L} \sum_{m=-\ell}^{\ell} {B_r}_\ell^m(r_c) Y_\ell^m(\theta, \phi), \tag{15}$$

noting that we have already truncated the expansion according to the native resolution of the CE dynamo model. We can now connect each coefficient of this expansion with the poloidal scalar introduced above

$${B_r}_\ell^m(r_c) = \frac{\ell(\ell+1)}{r_c} \mathcal{P}_\ell^m(r_c), \tag{16}$$

which then allows us to write formally the link between $\mathcal{P}$ and the prediction for the datum Z,

$$Z(r_0, \theta_0, \phi_0) = \frac{1}{2r_c} \sum_{\ell=1}^{L} \sum_{m=0}^{\ell} \ell(\ell+1) \left[\mathcal{P}_\ell^m(r_c) {\mathcal{G}_Z}_\ell^{m\,\dagger} + \mathcal{P}_\ell^{m\,\dagger}(r_c) {\mathcal{G}_Z}_\ell^m\right], \tag{17}$$

where we have now restricted the sum to positive values of m only, and consequently introduced the † for conjugation (Z is real-valued). In this expression, ${\mathcal{G}_Z}_\ell^m$ is the coefficient of degree ℓ and order m of the SH expansion of $G_Z(r_0, \theta_0, \phi_0 | r_c, \theta, \phi)$. The linear observation operator for a Z measurement, $\mathbf{H}_Z$, can then be defined as

$$\mathbf{H}_Z = \frac{1}{2r_c} \left[\ldots, \ell(\ell+1) {\mathcal{G}_Z}_\ell^{m\,\dagger}, \ldots, \ell(\ell+1) {\mathcal{G}_Z}_\ell^m, \ldots\right], \tag{18}$$

which is applied to the expanded state vector $\mathbf{x} = [\ldots, \mathcal{P}_\ell^m, \ldots, \mathcal{P}_\ell^{m\dagger}, \ldots]^T$, where m can only take positive values. The same formalism can be applied in order to define the operators $\mathbf{H}_X$ and $\mathbf{H}_Y$ for the North and East measurements of the magnetic field, respectively.

A considerable amount of data from the past magnetic field consists of indirect and often incomplete information about the magnetic field vector. Such information is given in terms of the directions, declination D and inclination I of the vector, or intensity F. The directions and intensity are nonlinear combinations of the magnetic field vector components (X, Y, Z),

$$D = \arctan \frac{Y}{X}, \tag{19}$$

$$I = \arctan \frac{Z}{\sqrt{X^2 + Y^2}}, \tag{20}$$

$$F = \sqrt{X^2 + Y^2 + Z^2}. \tag{21}$$

To calculate the linearized observation operator given by eq. (4), we have to bear in mind that in practice, this operator achieves a mapping from the complex-valued $\mathbf{x}$ to a real-valued measurement. The details of the derivation of the linearized observation operators for D, I and F data are given in Appendix.

2.5 An ensemble approach

We finish this methodological preamble by explaining how we define in practice the background state $\mathbf{x}^b$ and the background error covariance matrix $\mathbf{P}^b$ which must be supplied to the iterative algorithm. We resort to an ensemble of N_e state vectors $\mathbf{x}_e$ taken randomly from a 100 000-yr long integration of the coupled Earth dynamo model. Our estimator is the ensemble mean, and the background state is therefore the average of these N_e states,

$$\mathbf{x}^b = \frac{1}{N_e} \sum_{e=1}^{N_e} \mathbf{x}_e. \tag{22}$$

As already stated above, we take $N_e = 820$ such states in order to get statistical convergence. Let us recall that $\mathbf{x}^b$ is a complex-valued field

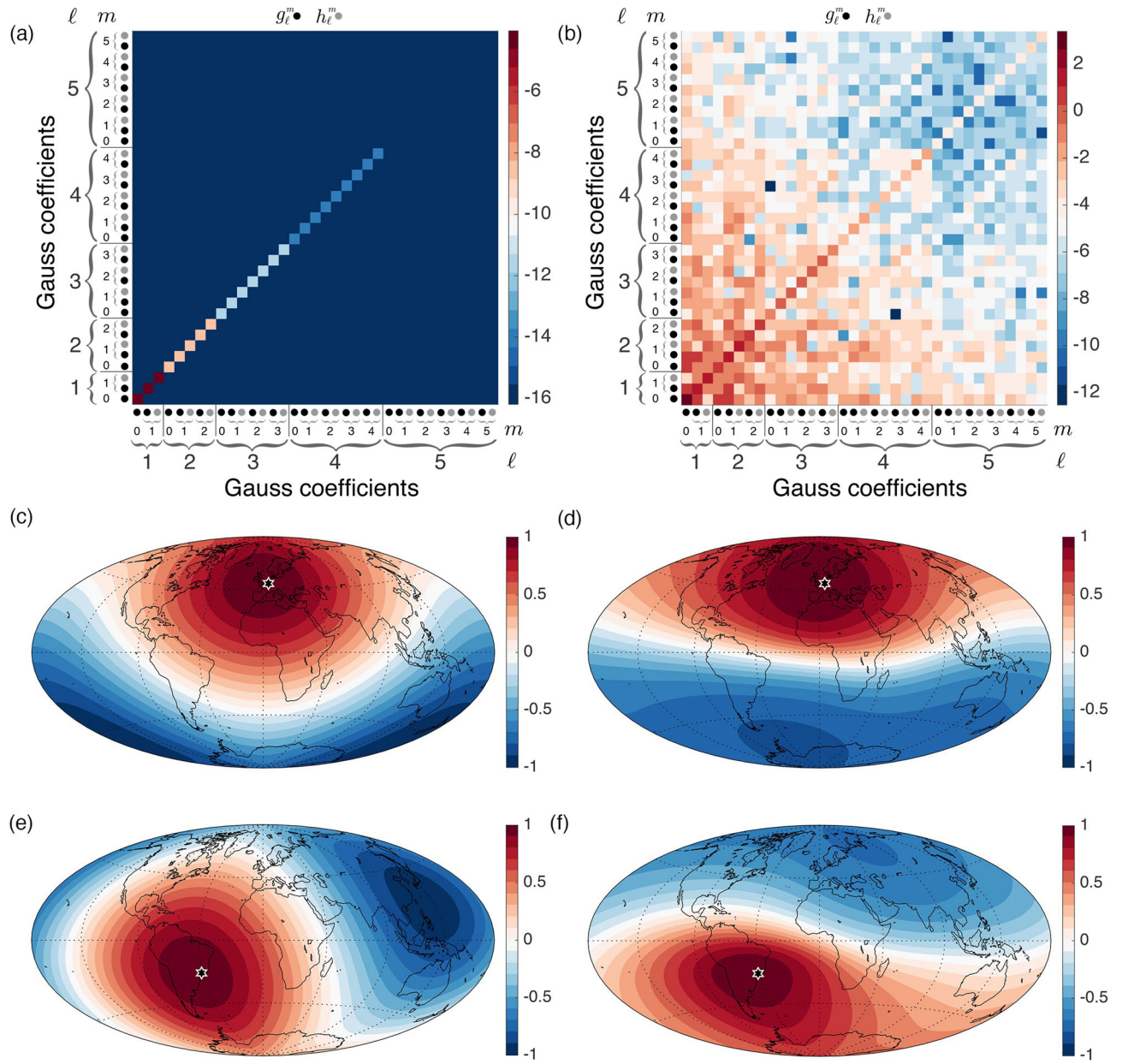

Figure 2. Covariance matrices and spatial correlations implied by the prior information between the radial magnetic induction at different core surface points. Top row: covariance between the different Gauss coefficients up to degree 5 from (a) the 'dissipation' norm and (b) the CE dynamo simulation. Both covariance matrices are shown in logarithmic scale and in μT^2. Middle row: spatial correlations underneath Paris (shown with the star) and any point on the core surface for (c) prior information supplied by the dissipation norm and for (d) prior information supplied by the CE dynamo. Bottom row: same, save that the correlations are expressed with respect to a point underneath São Paulo for (e) the dissipation norm prior and (f) the CE dynamo norm prior.

containing the SH representation of the poloidal scalar at the core surface. We therefore define the background covariance matrix as

$$\mathbf{P}^b = \frac{1}{N_e - 1} \sum_{e=1}^{N_e} \left(\mathbf{x}_e - \mathbf{x}^b\right) \left(\mathbf{x}_e - \mathbf{x}^b\right)^{\dagger T}, \tag{23}$$

noting that $\mathbf{P}^b$ is a complex-valued, Hermitian matrix.

Implicit is the assumption that these two moments suffice to characterize the prior information. This is only true, however, when dealing with Gaussian statistics. Previous studies indicate that the large-scale magnetic field produced by a buoyancy-driven dynamo is indeed close to possess Gaussian statistics (Fournier *et al.* 2011, their fig. 4).

In order to gain insight into the type of prior information supplied by $\mathbf{P}^b$ and compare it with the prior based on the Ohmic dissipation approximation $\mathbf{C}$ of Bloxham *et al.* (1989), recall eq. (7) above, we show in the first row of Fig. 2 the covariance matrices corresponding to both cases. We can see in Fig. 2(a) that $\mathbf{C}$ is diagonal, and depends only on the SH order ℓ. On the contrary, $\mathbf{P}^b$ in Fig. 2(b) displays a high amount of correlation between the different model variables, depending also on the SH order m. We further introduce the linear operator $\mathbf{M}$ which maps $\mathbf{x}$ to a vector $\mathbf{v}_B$ containing the values of B_r on a grid approximating the core surface,

$$\mathbf{v}_B = \mathbf{M}\mathbf{x}. \tag{24}$$

In this way, we can project the information from the covariance matrices contained in spectral space into physical space, by means of a matrix $\mathbf{W} \equiv \mathbf{M}\mathbf{P}^b\mathbf{M}^{\dagger T}$. We can then express the correlation ρ_{ij} between B_r at the i-th grid point and B_r at the jth grid point as follows

$$\rho_{ij} = \frac{W_{ij}}{\sqrt{W_{ii}W_{jj}}}. \tag{25}$$

Figs 2(d) and (f) show mappings of the correlations given by ρ between core surface grid-points at specific locations (Paris and São Paulo) and every grid-point of the CMB based on $\mathbf{P}^b$. For comparison, Figs 2(c) and (e) also show these correlations when the dynamo-based $\mathbf{P}^b$ is replaced by the minimum dissipation matrix $\mathbf{C}$. The prior information supplied by the CE dynamo favours antisymmetry with respect to the equator, whereas the dissipation norm implies correlations whose geometry reflects that of an inclined dipole piercing through Paris or São Paulo. The different prior correlations will impact the way information from the observations are propagated among the model variables when constructing the global models (eq. 1).

The posterior covariance is calculated by solving the iterative algorithm for each member of the ensemble, as would be required in a sequential data assimilation framework based on the EnKF (e.g. Evensen 2003). If $\hat{\mathbf{x}}_e$ denotes the estimate for each ensemble member e, then one can get $\hat{\mathbf{P}}$ by computing

$$\hat{\mathbf{P}} = \frac{1}{N_e - 1}\sum_{e=1}^{N_e}(\hat{\mathbf{x}}_e - \hat{\mathbf{x}})(\hat{\mathbf{x}}_e - \hat{\mathbf{x}})^{\dagger T}, \tag{26}$$

where $\hat{\mathbf{x}}$ is the estimator (the mean). For that expression to give a $\hat{\mathbf{P}}$ equal to the one provided by eq. (5), the iterative algorithm to apply to each initial $\mathbf{x}_e$ must write

$$\mathbf{x}_e^{k+1} = \mathbf{x}_e + \mathbf{P}^b\mathbf{H}^{k\dagger T}\left(\mathbf{H}^k\mathbf{P}^b\mathbf{H}^{k\dagger T} + \mathbf{R}\right)^{-1} \times \left[\mathbf{y} + \epsilon_e - \mathcal{H}\left(\mathbf{x}^k\right) + \mathbf{H}^k\left(\mathbf{x}^k - \mathbf{x}_e\right)\right], \tag{27}$$

where $\mathbf{x}^k$ is the ensemble mean at the k-th step of the algorithm, and $\mathbf{H}^k$ is the observation operator linearized about this ensemble mean. Note that for each ensemble member, the data are noised by an amount ϵ_e drawn from a normal distribution of zero mean and covariance $\mathbf{R}$ (Burgers *et al.* 1998).

Finally, let us note that instead of opting for a linearized approach, one could simply compute each state estimate $\hat{\mathbf{x}}_e$ using the nonlinear observation operator, according to

$$\hat{\mathbf{x}}_e = \mathbf{x}_e + \left(\mathbf{H}\mathbf{P}^b\right)^{\dagger T}\left(\mathbf{H}\mathbf{P}^b\mathbf{H}^{\dagger T} + \mathbf{R}\right)^{-1}\left[\mathbf{y} + \epsilon_e - \mathcal{H}\left(\mathbf{x}_e\right)\right], \tag{28}$$

with

$$\mathbf{H}\mathbf{P}^b = \frac{1}{N_e - 1}\sum_{e=1}^{N_e}\left[\mathcal{H}(\mathbf{x}_e) - \mathcal{H}\left(\mathbf{x}^b\right)\right]\left[\mathbf{x}_e - \mathbf{x}^b\right]^{\dagger T}, \text{ and} \tag{29}$$

$$\mathbf{H}\mathbf{P}^b\mathbf{H}^{\dagger T} = \frac{1}{N_e - 1}\sum_{e=1}^{N_e}\left[\mathcal{H}\left(\mathbf{x}_e\right) - \mathcal{H}\left(\mathbf{x}^b\right)\right]\left[\mathcal{H}\left(\mathbf{x}_e\right) - \mathcal{H}(\mathbf{x}^b)\right]^T \tag{30}$$

computed based on the ensemble of states. This strategy has the advantage of expediency, since it only requires one iteration. In the context of archaeomagnetism, it appears to be slightly less accurate than the iterative one (see Section 2.6 below).

2.6 Validation

With archaeomagnetic applications in mind, we proceed with a simple test considering the retrieval of the large scales of the magnetic field at the CMB from synthetic data. The synthetic data set consists of magnetic data at 35 locations spread in a close-to-uniform fashion at Earth's surface, a nearly ideal (and admittedly unrealistic) scenario for the distribution of archaeomagnetic data, shown in Fig. 3(a). The number of data locations corresponds to the amount of full vector observations necessary to recover the magnetic field up to SH degree $L = 5$ (35 Gauss coefficients). A reference model state $\mathbf{x}^t$ is used to produce synthetic vector observations at the given locations, to which a 1 μT value is introduced for the data uncertainty. The (X, Y, Z) observations are transformed into (D, I, F) and the uncertainties are propagated and noised with a random component drawn from a normal distribution (whose standard deviation is obtained from the uncertainty propagation). The observation error covariance matrix $\mathbf{R}$ is diagonal, with each diagonal element equal to the variance of each synthetic observation.

In order to quantify the efficacy of the scheme we use three diagnostics for the estimates: the normalized data misfit

$$M(\mathbf{x}) = \sqrt{\frac{1}{n_\mathbf{y}}\left[\mathbf{y} - \mathcal{H}(\mathbf{x})\right]^T\mathbf{R}^{-1}\left[\mathbf{y} - \mathcal{H}(\mathbf{x})\right]}, \tag{31}$$

the normalized spread (i.e. the standard deviation) of the ensemble

$$S(\mathbf{x}_e) = \sqrt{\frac{1}{n_\mathbf{x}}\frac{1}{N_e - 1}\sum_{e=1}^{N_e}(\mathbf{x}_e - \langle\mathbf{x}_e\rangle)^{\dagger T}\mathbf{P}_d^{b\,-1}(\mathbf{x}_e - \langle\mathbf{x}_e\rangle)}, \tag{32}$$

and the normalized error with respect to the known true state $\mathbf{x}^t$

$$E(\mathbf{x}) = \sqrt{\frac{1}{n_\mathbf{x}}(\mathbf{x} - \mathbf{x}^t)^{\dagger T}\mathbf{P}_d^{b\,-1}(\mathbf{x} - \mathbf{x}^t)}, \tag{33}$$

where $\mathbf{P}_d^b$ is the diagonal matrix assembled from the diagonal elements of $\mathbf{P}^b$. It is important to note that the spread and error are evaluated throughout this paper up to SH degree 5, that is, over that part of the state vector which is effectively constrained by observations (as will be clear in Section 3.3). The evolution of these quantities with iteration count can be seen in Fig. 4, which shows that the algorithm converges after three iterations. The misfit M decreases from 5 to around 0.8 with the iterative scheme and 0.95 with the nonlinear one described at the end of Section 2.5, which points to the better fit to the data set of the iterative solution. The iterative solution is also slightly superior in terms of spread S and error E, which represent the uncertainty level of the model and its distance with respect to the truth, respectively. It is interesting to note the agreement of 20 per cent for the final estimates of S and E, suggesting that the ensemble spread is a good proxy for the posterior model error. Additionally, the fast convergence of the iterative scheme indicates the weak nonlinear character of the problem at hand, which gives us confidence in the ability of the algorithm to deal with the true archaeomagnetic data set and validates the interpretation of the resolution matrix defined in eq. (6).

The resolution matrix for the data set displayed in Fig. 3(a) is close to identity, implying that the data resolve very well the model coefficients due mainly to their good spatial distribution. In the case of a biased spatial distribution of the data, the matrix also comprises non-diagonal elements, which hints to the non-uniqueness of the problem. Still, the diagonal elements are sufficient to assess the resolution. For simplicity, we will discuss throughout this paper the information contained in the resolution matrix in terms of its

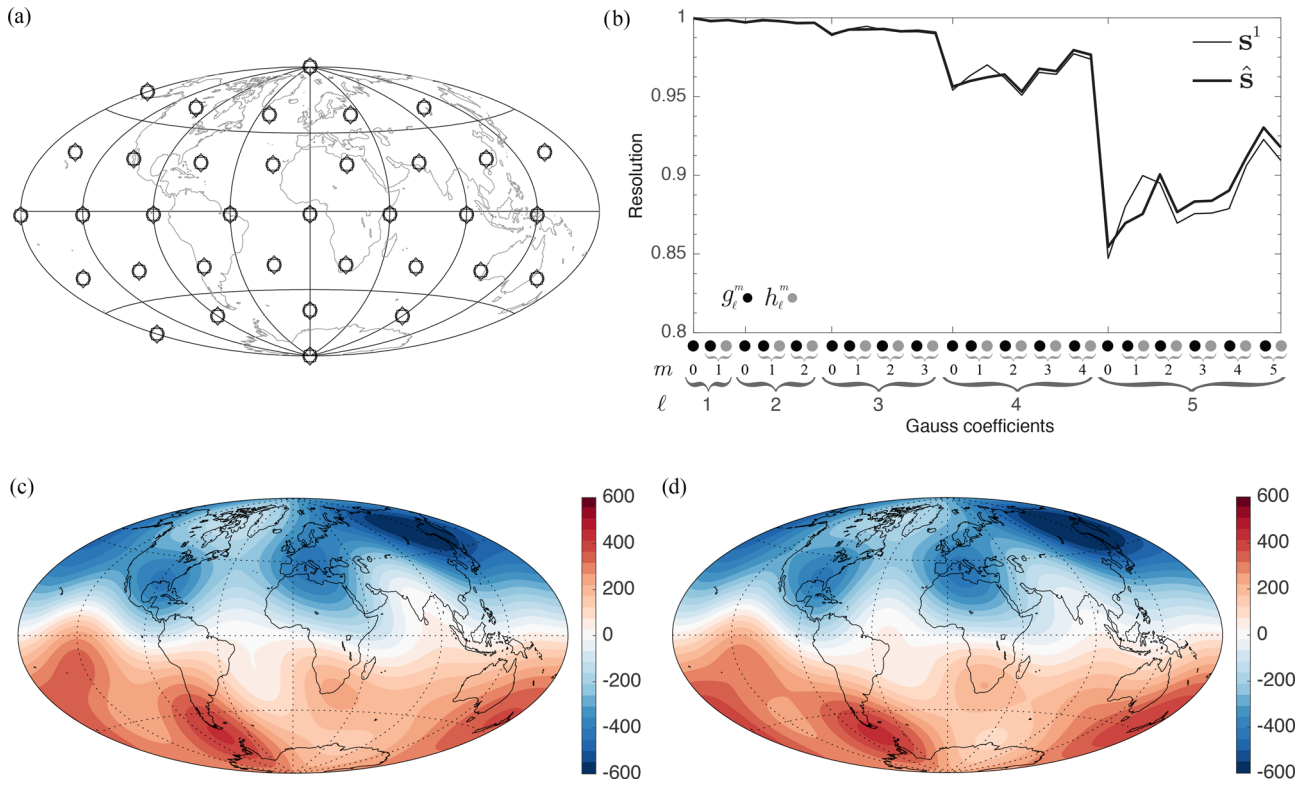

Figure 3. Synthetic directional and intensity data set, its resolution in model and physical space. (a) Distribution of synthetic observations at Earth's surface; (b) resolution of Gauss coefficients up to degree 5. (c) Magnetic field at the CMB characterizing the reference or 'true' state and (d) the final estimate of the magnetic field at the CMB given the close-to-uniform distribution of surface data (units in μT). See the text for details.

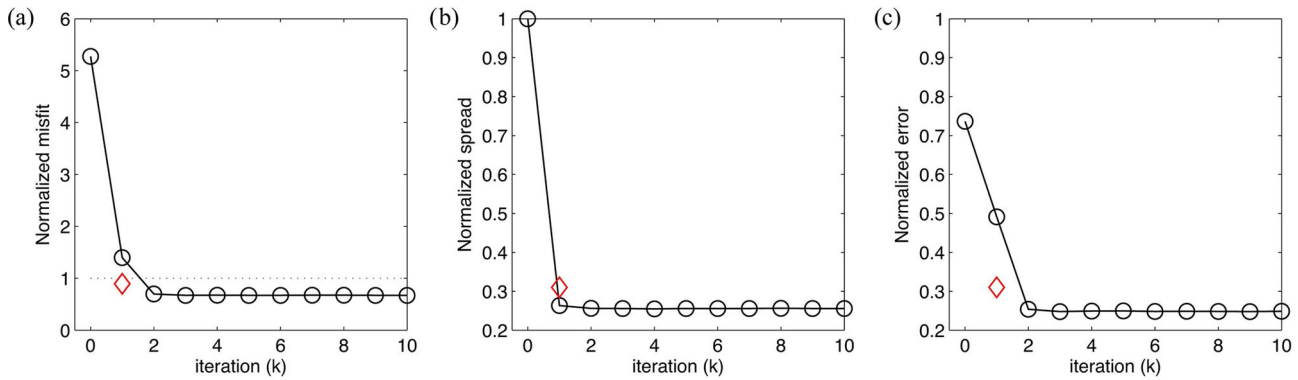

Figure 4. Convergence of the iterative solutions for the validation test in terms of normalized (a) misfit, (b) spread of the ensemble and (c) error of the mean estimate. The black curve shows the iterative estimates by means of the linearized observation operator approach, while the red diamond corresponds to the nonlinear observation operator-based analysis. See the text for details.

diagonal elements only. Since the resolution matrix of eq. (6) represents the ratio between the covariances in the background model and data ($\hat{S}_i \approx {\sigma_i^b}^2/({\sigma_i^b}^2 + {\sigma_y}^2)$ for a model state variable i), we analyse our results in terms of its square-root $\hat{\mathbf{S}}^{1/2}$, thereby dealing with standard deviations instead of variances. Projecting the diagonal elements of the square-root of the resolution matrix into Gauss coefficients through the $\mathbf{Q}$ operator introduced in Section 2.3, we can introduce a resolution vector $\hat{\mathbf{s}}$ constructed from the diagonal elements of $\mathbf{Q}\hat{\mathbf{S}}^{1/2}\mathbf{Q}^{\dagger T}$. We show this resolution vector up to degree 5 in Fig. 3(b). Also plotted is the resolution vector at the first iteration $\mathbf{s}^1$, which closely resembles the resolution vector of the final estimate, $\hat{\mathbf{s}}$. The resolution vector coefficients are of order unity up to degree 3, meaning that the data constrain the corresponding Gauss coefficients almost to 100 per cent. Degree 4 and 5 are constrained up to 97 per cent and 90 per cent, respectively. The relative lack of resolution of the $m = 0$ zonal coefficients (such as g_4^0 and g_5^0), reflects the small amount of data underneath polar regions, precisely where associated Legendre functions of order 0 reach their maximum amplitudes. Since the resolution vector is seen not to change considerably from the first to the last iteration, we will consider the resolution vector at the first iteration, $\mathbf{s} = \mathbf{s}^1$, as representative of the model resolution throughout this paper. The interest in this choice is that $\mathbf{s}^1$ depends only on the data and prior information, allowing us to analyse the resolution before performing the iterative estimation per se.

The sum of the elements of the vector $\hat{\mathbf{s}}$, corresponding to the trace of the square-root of the resolution matrix, is 33. This figure

corresponds to the number of resolved degrees of freedom of the model given the data set in question, comparable to SH degree 5. This result can be confirmed by the comparison between the reference state (from which the synthetic observations were generated) shown in Fig. 3(c), and the estimate retrieved by means of the observations shown in Fig. 3(d) truncated to SH degree 5.

Note that an independent validation of the results discussed in this paragraph was carried out by a brute force calculation of the tangent observation operators, for a state vector made directly of Gauss coefficients. The weakly nonlinear character of the problem at hand, as well as the satisfactory behaviour of the scheme in this simple test prompt us to exercise it further in the more realistic and challenging context of archaeomagnetic observations.

3 ARCHAEOMAGNETIC RESOLUTION ANALYSIS

3.1 Archaeomagnetic database

The archaeomagnetic data set used in this proof-of-concept paper relies on the Geomagia50.V2 database (Donadini *et al.* 2009) for the period from 1200 BC to 2000 AD. Geomagia50.V2 consists of directional and intensity data spanning the past 50 millennia that derive from the analysis of the remanent magnetization carried by volcanic deposits and archaeological artefacts, like bricks, pottery, ovens, etc. This version of the database is not the newest one, but is sufficiently mature to help illustrate the fundamental aspects of the method we designed. Using it allows us to compare our findings with models previously published relying on practically the same data set.

The data set clearly shows that the available archaeomagnetic data present a very uneven temporal and geographical distribution. Spatially, most of the data are located in Western Eurasia. In fact, almost all observations are located in the Northern Hemisphere, with just 2.5 per cent of the data in the Southern Hemisphere (Donadini *et al.* 2009; Licht *et al.* 2013). At any given epoch, we therefore rely on the prior information supplied by the dynamo to recover the field behaviour in the Southern hemisphere, based on the spatial correlations of the prior (recall Figs 2a and c). Regarding the data, we follow a hybrid strategy based on Korte *et al.* (2009) and Licht *et al.* (2013) in order to better compare the different models, attributing lower bounds for the data uncertainties and asserting uncertainties to data without such information. We arbitrarily choose a lower bound of 2 μT for intensity data uncertainties and 3.4° for the α_{95} parameter uncertainties, following the modelling errors assigned by Licht *et al.* (2013) as a consequence of the degree 5 truncation of their modelling strategy. This implies a lower bound for the standard deviation of $\sigma_I = (81/140) \times 3.4^\circ$ for the inclination I and $\sigma_D = (81/140 \cos I) \times 3.4^\circ$ for the declination D. Data with no uncertainty information are assigned an uncertainty of 8.25 μT for intensity and 4.5° for α_{95}, which amounts to 150 per cent of the average of known uncertainties, following Licht *et al.* (2013).

With regard to ages, results are dated either by radiogenic techniques, often the case for volcanic data, or by means of archaeological constraints, in the case of archaeological artefacts. These different dating techniques result in different probability density functions (pdf) for the age, Gaussian for radiogenic dating or uniform for archaeological dating (e.g. Ramsey 2009). Age uncertainties have been treated in different ways in archaeomagnetic field modelling. The most recent global models of Korte & Constable

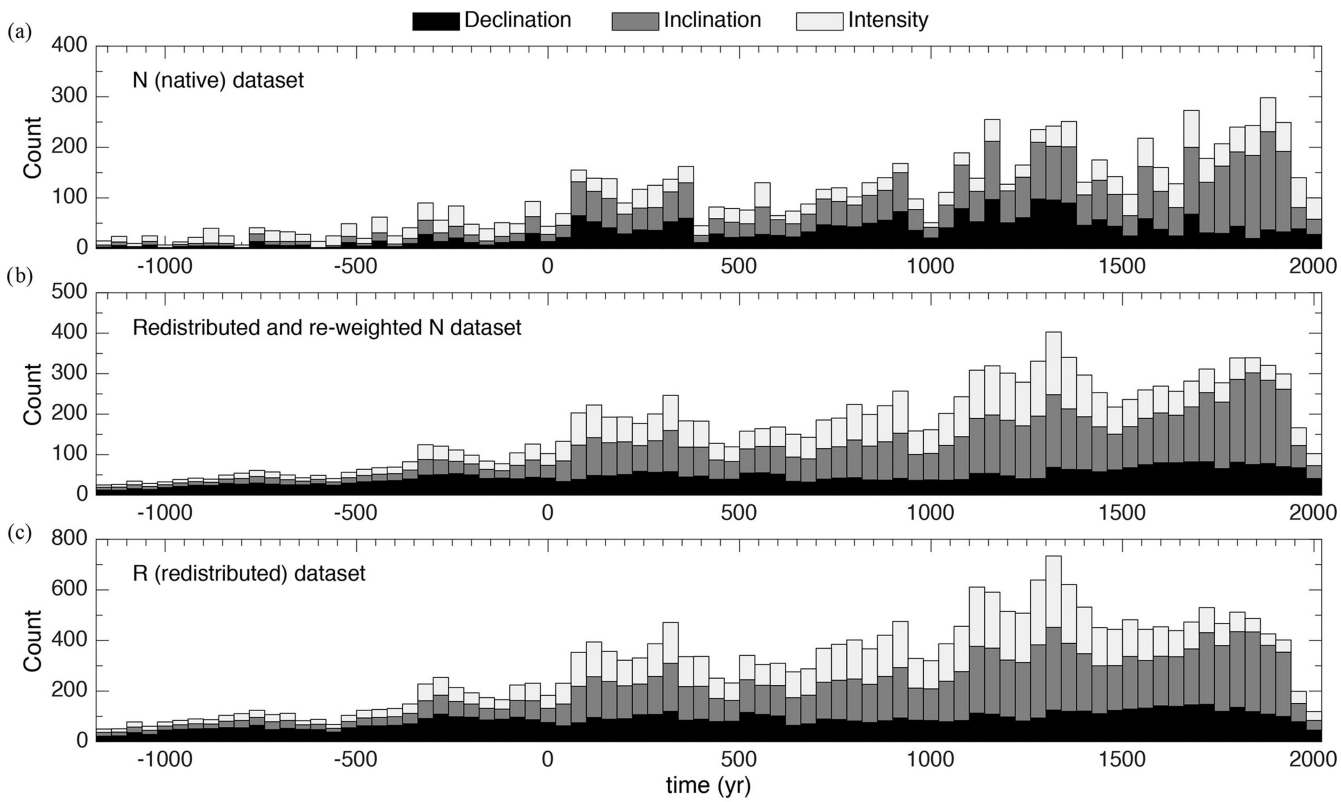

Figure 5. Histograms of the archaeomagnetic data sets used in this study. (a) The native (N) data set constructed from Geomagia50.V2 (Donadini *et al.* 2009); (b) redistribution of the N data set given the re-weighting based on the probability density function of the age of each datum, counted by their weights; (c) the redistributed (R) data set, which assumes that the redistributed data are independent, with a recalibrated measurement uncertainty. See the text for details.

(2011), Licht *et al.* (2013) and Pavón-Carrasco *et al.* (2014) use different flavours of bootstrap sampling to account for errors in age estimations (jointly with measurement errors), while, in a regional context, Hellio *et al.* (2014) resort to a Monte Carlo Markov Chain to sample the space of possible ages of a regional data set.

In the single-epoch approach outlined in this study, we do not treat the archaeomagnetic field model temporal dependency. Instead, we group the data within bins of 40-yr width, assuming that the field is constant over that period. The width of 40 yr is a compromise between the shortest time possible (for the assumption of steadiness to hold) and the longest one, which will favour a larger number of data (and should therefore improve the accuracy of the model). Over 40 yr, one can expect that the harmonic components of the field of degree $\ell \leq 5$ will not undergo significant changes, since their typical time scales τ_ℓ are thought to vary like $\tau_\oplus/\ell$, with a master SV coefficient $\tau_\oplus$ of order 400 yr (Lhuillier *et al.* 2011).

3.2 Data redistribution based on age uncertainties

A first data set can be constructed by taking the mean age of each datum, ignoring the age uncertainties, and rejecting these data for which the age uncertainty is either not provided or is strictly larger than $\pm$100 yr (total 200 yr). 1633 data were rejected within this criterion, corresponding to 16 per cent of the original data set. Such selected and reworked Geomagia50.V2 data set is labelled here as the N (native) data set. Fig. 5(a) shows the histogram of the N data set comprising 2528 declination, 3757 inclination and 2230 intensity data distributed within the 40-yr bins through the time interval from 1200 BC to 2000 AD, with thus a total of 8515 data.

Within our snapshot framework, a possibility to deal with age uncertainties would be to draw an ensemble of data sets based on the age pdf of each datum, and to apply our framework to each draw. The final archaeomagnetic field model (for each time bin) would then consist of a weighted average of the ensemble of models, following the procedure detailed by Lanos (2004) for the construction of regional archaeomagnetic curves. Although we are planning to use that strategy in the future, we opt here for a more expedient (and less accurate) strategy of redistribution, whereby each datum is distributed in the bins where its age pdf is not zero, with a weight given by the pdf integrated over each bin. For a given datum, the reworked uncertainty inside the jth bin b_j, defined by the time window $[t_i(b_j), t_f(b_j)]$, is described by

$$\sigma_{b_j} = \sigma_o \times w_{b_j}^{-1/2}, \tag{34}$$

where σ_o is the original uncertainty of the data and the weight w_{b_j} is defined by

$$w_{b_j} = \int_{t_i(b_j)}^{t_f(b_j)} f(\sigma_t, t_o, t)\mathrm{d}t, \tag{35}$$

where $f(\sigma_t, t_o, t)$ is a function representing the pdf associated with the datum's age uncertainty σ_t (Gaussian or boxcar), t_o is the expected age and t is time. If the redistributed data are counted with respect to their new weights in each bin, the result is a smoother distribution of the N data set, as can be seen in Fig. 5(b). The data redistribution and uncertainty re-weighting of the native N data set leads to a new data group, called R (for redistributed) henceforth. If each redistributed datum in each bin is considered as a discrete independent datum, the R data set comprises 7432 declination, 10 055 inclination and 6904 intensity data, for a total of 24 391 data, whose histogram is shown in Fig. 5(c).

Although the present archaeomagnetic field estimation method does not include a regularization of the model in time, it is important to remark that the grouping of data in 40-yr bins, the assignment of lower bounds to the uncertainties and the further redistribution of the data set (meaning the transformation of N into R), act effectively as a temporal regularization.

3.3 Resolution of the archaeomagnetic data set

Before applying our iterative scheme to the N and R archaeomagnetic data sets, let us analyse the impact of the data under consideration on our knowledge of the magnetic field at the core surface. The issue of archaeomagnetic data resolution has been addressed, among other authors, by Korte & Constable (2008) and Licht *et al.* (2013). The authors suggested, by means of comparing the power spectra from archaeomagnetic, historical and satellite data-based models, that archaeomagnetic field models are resolved approximately up to SH degree 4. However, a careful quantification of the archaeomagnetic resolution and its variability in time has not yet been performed, mostly due to the difficulty in calculating the resolution matrix for continuous models. We have seen in Section 2.1 that the resolution matrix given by eq. (6) quantifies the influence of the properties of the data set on the model. For simplicity, we present the resolution vector $\mathbf{s}$ after the first iteration (recall the end of Section 2.6) to synthesize the information contained in the matrix and to represent the resolving power of the archaeomagnetic data set in each 40-yr interval from 1200 BC to 2000 AD.

The resulting sequence of resolution vectors, which we will call the archaeomagnetic resolution matrix throughout, represents the evolution of the archaeomagnetic resolution in time, and is shown in Fig. 6 for both the N and R data sets. The similarity between both matrices in Figs 6(a) and (b) in terms of amplitude and behaviour shows that the increase of the uncertainties by the data re-weighting of data set R is mitigated by the increase in the number of data. The smoother character of the R-based resolution matrix is a consequence of the better distribution of the data given their age uncertainties information, and therefore, of its effective temporal regularization.

The key aspect of Fig. 6 is that it demonstrates the inability of the archaeomagnetic data set here considered to resolve the magnetic field at the core surface for spatial scales beyond SH degree 5. Due to the smoother character of the R data-set-based archaeomagnetic resolution matrix, the following description will focus on Fig. 6(b). For the whole 3000 yr interval, only the dipole and quadrupole are continuously well resolved. The axial dipole g_1^0 is the best constrained coefficient, resolved around 90 per cent from 1200 BC to 0 AD and up to almost 100 per cent from 0 AD to 2000 AD. The other components of the dipole, together with the quadrupole terms, evolve from roughly 70 per cent up to 85 per cent after 0 AD. The octupole ($\ell = 3$) shows a resolution of 50 per cent before 0 AD, while after 0 AD the resolution increases up to around 75 per cent at present-day. The degree 4 starts presenting resolution lows, meaning that at times the resolution of some coefficients is lower than an arbitrary value of 30 per cent. The period after 0 AD presents a reasonable resolution of 50 per cent for degree 4 and after 1000 AD a resolution around 40 per cent for degree 5. Beyond degree 5 the model variables display little to no sensitivity to the data sets. For all coefficients of degree higher than the quadrupole, the general rule is that the zonal modes ($m = 0$), are not well constrained within the corresponding degree, due to the lack of observations in polar regions. In contrast, sectoral modes ($m = \ell$) are best resolved within a

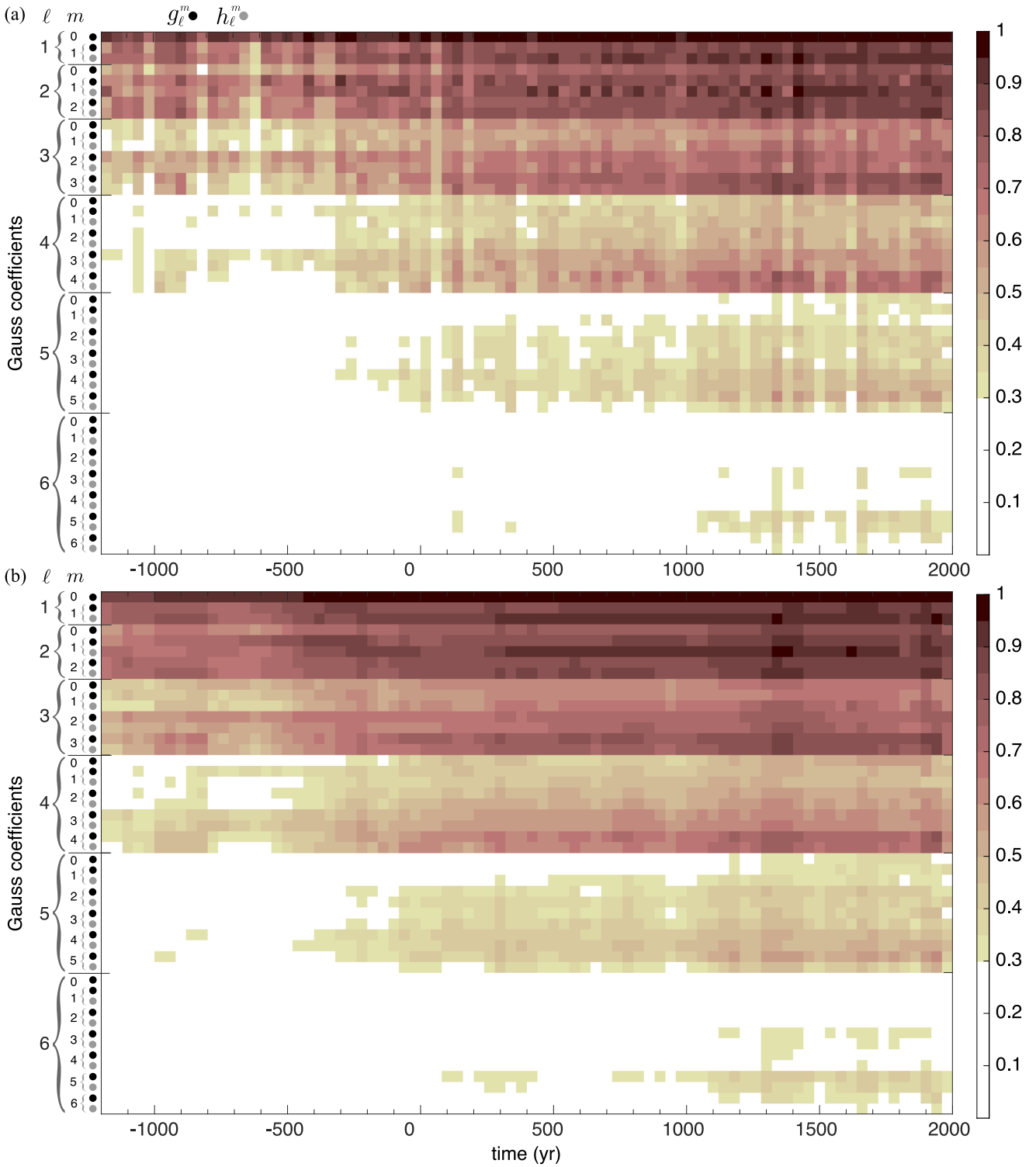

Figure 6. Archaeomagnetic resolution matrices, given the Coupled Earth dynamo prior and (a) the N or (b) the R data set. The colour scale represents the normalized resolving power of the data on the model state variables, cast here in terms of Gauss coefficients, up to spherical harmonic degree 6.

given harmonic degree family, due to their better sampling of lower latitudes, which coincides with the data spatial distribution.

In synthesis, we observe a good resolution of the archaeomagnetic field up to degree 3 for the period between 1200 BC and 0 AD, degree 4 from 0 AD to 1000 AD, and degree 5 from 1000 AD onwards. The trend corresponding to the increase in resolving power in time contained in both matrices is related mainly to the increase of data availability in the interval, as can be seen by comparing Figs 5(a) and 6(a) and Figs 5(c) and 6(b). Attention must be drawn to the fact that the N and S resolution matrices are based on an outdated version of the GEOMAGIA database. The upgrades from the newest version of the GEOMAGIA compilation, which do not significantly alter our observations mentioned above, are discussed in Section 5. It is also important to note that the archaeomagnetic resolution

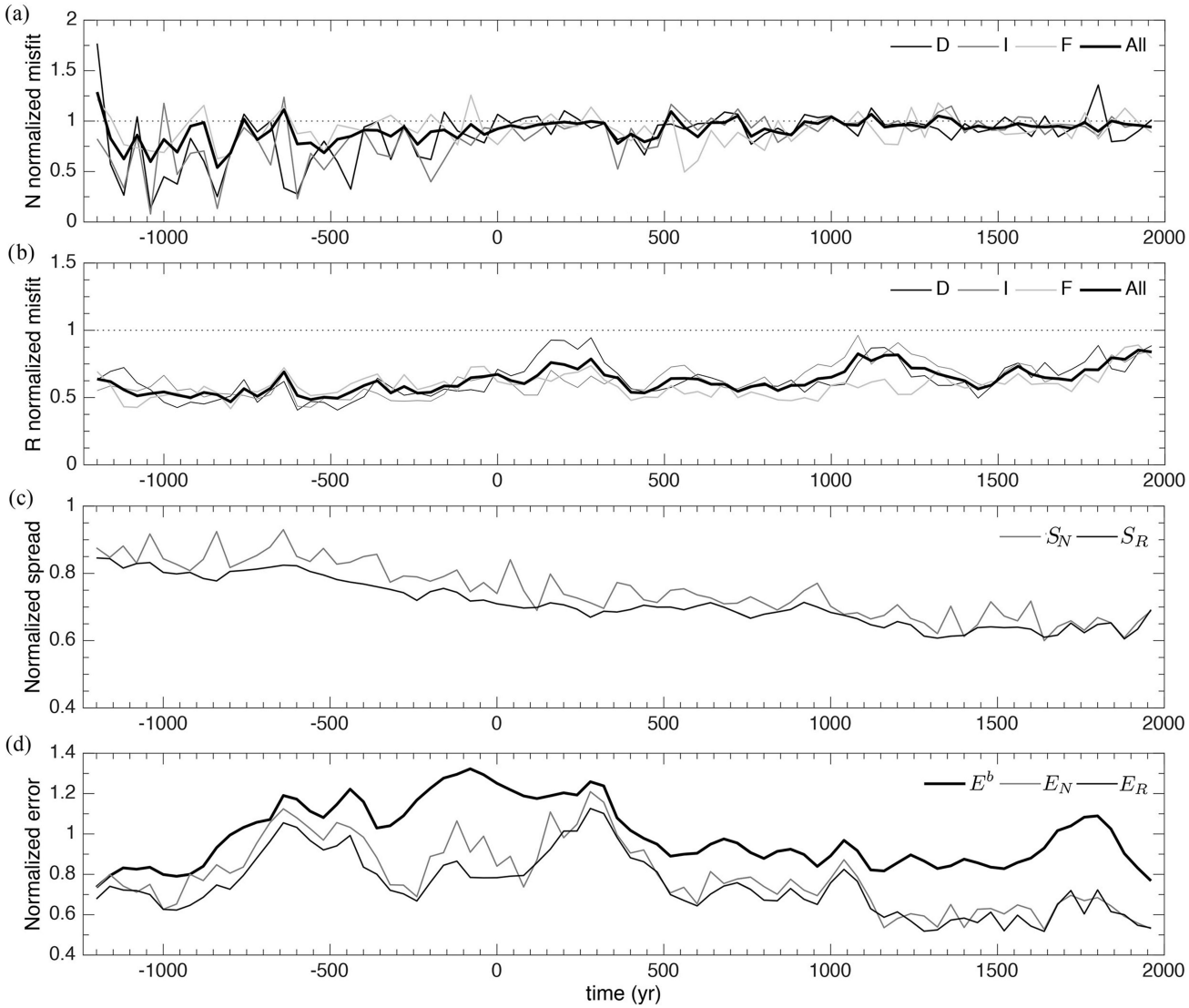

Figure 7. Diagnostics of the twin experiments in terms of (a) the normalized misfit M of the final estimation for the synthetic N data set, (b) normalized misfit M of the final estimate for the synthetic R data set, (c) normalized total spread S for both estimates and (d) the normalized total error E of the background and final estimate for the synthetic N and R data sets. Note that S and E are calculated considering a degree 5 truncation.

matrices shown in Fig. 6 represent an idealization of the model resolution by the data, in the sense that they do not depend on data values themselves, and therefore, do not consider the existence and impact of incoherent data, which are likely to be present in the real archaeomagnetic data set (e.g. Licht *et al.* 2013). In order to test the robustness of the conclusions drawn from the analysis of the archaeomagnetic resolution matrices and to prepare the application of the scheme to real data sets, we next design archaeomagnetic twin experiments, whereby we can directly assess error on the state estimates based on synthetic analogues of the N and R data sets.

3.4 Twin experiments

In this twin experiment, like in the validation test of Section 2.6, synthetic data are generated from a reference model simulation, the 'true' state, which can be directly compared with the estimates of the iterative scheme. The true state evolves in time, since it is the product of the integration of the coupled Earth dynamo, and for each 40-yr interval it is calculated as the average over 40 yr of this integration. In this case, the two archaeomagnetic data sets N and R are tested to assess the validity of the data regularization by the redistribution and re-weighting based on the ages uncertainties. The synthetic observations are based on the original mean age, geographical distribution and age and data uncertainties from the two real data sets. The observations are further noised based on a random draw from the data uncertainty distribution. The noisy synthetic observations are then used to estimate the true state given the background model.

We proceed with the iterative estimation by applying an outlier rejection scheme, whereby data with misfits larger than 3 standard deviations after the first estimation are discarded. A second estimation is then produced with the remaining data set. Following this strategy, 22 data were excluded from the N data set (12 declination, 4 inclination and 6 intensity data) while 12 data were rejected from the R one (8 declinations and 4 inclinations).

The quality assessment of our estimates is made by using the three diagnostics introduced in Section 2.6, namely the normalized data misfit M, the normalized spread of the ensemble S and the normalized error E. Those are shown in Fig. 7. Fig. 7(a) reveals a

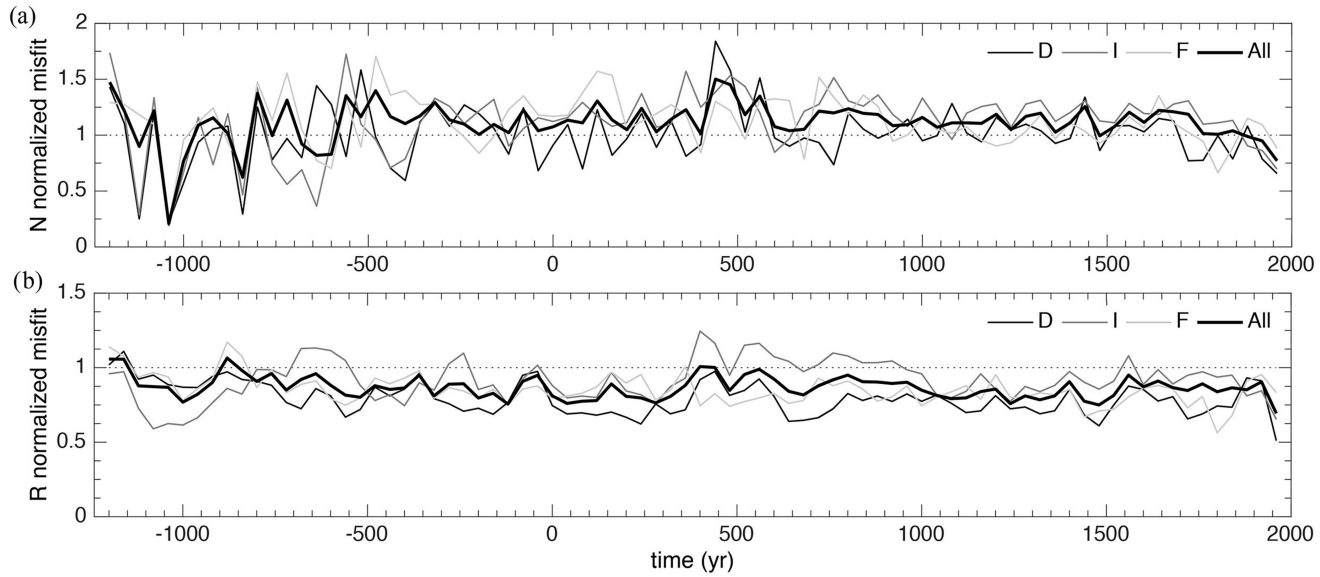

Figure 8. Normalized misfit M for (a) the N and (b) the R data set analysis.

mean misfit of 0.9 for the N-based estimate. Considering that the background mean misfit is close to 3 (based on the average field of Fig. 1a), the decrease amounts to 70 per cent. Further inspection of Fig. 7(a) indicates a stronger variability of the misfit during the first millennium BC than that prevailing since 0 AD. The R-based misfit shown in Fig. 7(b) reveals a mean of 0.6, which, compared to the background mean misfit of 1.75, reflects a decrease of 63 per cent. The smaller misfit values, and weaker variability of the R-based estimates compared with the N-based ones result from the increase in data uncertainties implied by the redistribution scheme.

The normalized spread S is shown in Fig. 7(c). The spread level is similar for both N and R-based estimates, around 85 per cent at the beginning of the interval, with an almost linear decrease down to 65 per cent at 2000 AD. This decreasing trend reflects the increase in data quantity with time (recall the histograms of Figs 5a and c). The spread of the R-based estimate displays a smoother variability than the N-based one.

Variations of the normalized error E are shown in Fig. 7(d). The background error E^b fluctuates since the true state dynamically evolves over the time interval, while the background state remains the same in our single-epoch analysis approach. E^b exhibits long-term millennial scale fluctuations, between 0.8 and 1.2. Although the normalized error for both N and R based estimations (E_N and E_R) presents an irregular behaviour through the interval, the mean error value decreases from 1 for E^b to approximately the same value of 0.8 for the N and R based estimations (interestingly, these values correspond to the mean values of the normalized spread we just discussed). The detailed temporal behaviour reflects the combination of the time-dependency of the true state on the one hand and of the varying distribution and quality of the data on the other hand. Sometimes, the initial guess (the background) is rather close to the truth, and the data does not strongly correct the estimate. In contrast, like at 0 AD and at 1800 AD, the initial guess is at times far from being optimal, and a substantial benefit is then drawn from the data.

4 STANDARD VERSUS DYNAMO-BASED ARCHAEOMAGNETIC FIELD MODELS

We now move to the application of our iterative approach to the real N and R archaeomagnetic data sets. Using the 3σ-rejection scheme discussed above, we discard 634 data from the N data set (114 declinations, 302 inclinations and 218 intensities) and 826 data from the R data set (136 declinations, 369 inclinations and 321 intensities). Fig. 8 shows the normalized misfit M for the final estimations based on the N and R data sets. We see in Fig. 8(a) that the N misfit does not differ substantially from that computed for the twin experiments, showing again a larger degree of variability during the first millennium BC (especially during its first half). The decrease from background to final estimation in misfit is of 57 per cent in this case, lower than that of the twin experiment. This lower performance in the misfit decrease indicates that the real archaeomagnetic data set is penalized by a number of data whose 'real' values lie outside their error bars. The R data set normalized misfit in Fig. 8(b) shows an almost constant value over the whole interval, as seen in the corresponding twin experiment in Fig. 7(b), albeit at an higher level (close to 0.9, to contrast with 0.6), and a decrease of 44 per cent in misfit. In summary, the differences between Figs 8 and 7 point to the presence of a certain amount of outliers in the archaeomagnetic data set (see also Licht *et al.* 2013).

As the error of the models cannot be directly assessed, we choose the estimate based on the smoother R data set as our reference model in order to compare it with inverse models built using a similar database (Geomagia50.V2). For convenience, we use the tag AmR to refer to our archaeomagnetic model based on the data set R and the CE dynamo background, and the tag Bm to refer to our background model. Figs 9 and 10 present groups of Gauss coefficients from AmR compared to models ARCH3k.1 from Korte *et al.* (2009) and A_FM-0 and A_FM from Licht *et al.* (2013). A brief description of the models is provided in the following:

ARCH3k.1: The ARCH3k.1 model consists of an inverse model built under adjustable temporal and spatial regularization truncated to degree 10 using lower bounds for data uncertainties (i.e. $\sigma = 5$ μT for intensities and $\alpha_{95} = 4.3^\circ$ for directions) and an outlier rejection scheme. The model is derived from an inversion beginning at 2000 BC, the product of which is not considered between 2000 BC and 1000 BC in order to avoid spurious spline-end effects. The opposite end of the model is drawn towards the *gufm1* model (Jackson *et al.* 2000) after 1650 AD for all non-axial dipole coefficients and after 1840 AD for the axial dipole coefficient. Since *gufm1* is

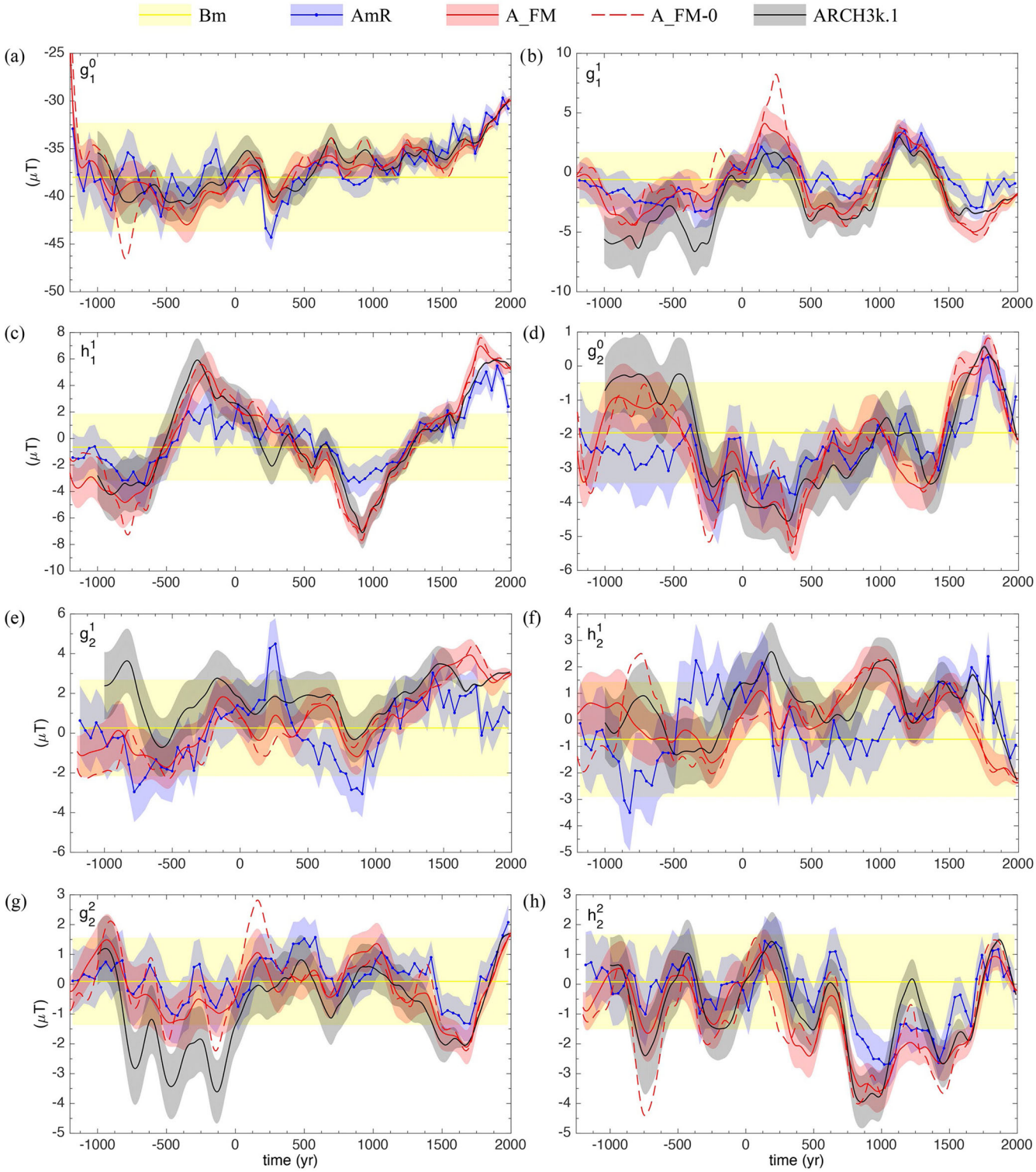

Figure 9. Gauss coefficients of the dipole and quadrupole magnetic field at the CMB. The background model Bm (yellow) is shown together with model AmR (blue). Both estimations are shown in terms of their mean and standard deviation calculated from the ensemble spread. Also shown are the AFM-0 model (red dashed curve), AFM-M model (red curve and shading) of Licht *et al.* (2013) and ARCH3k.1 model (black curve and shading) of Korte *et al.* (2009).

based on historical, observatory and satellite data, the last 500 yr of ARCH3k.1 result in a more precise estimate in comparison to the rest of the time interval. The model rests on a bootstrap to account for the different data set errors in order to provide a posteriori errors.

A_FM: The A_FM models are inverse models under the same general regularization approach as in ARCH3k.1. Acknowledging the fact that the available database does not allow to resolve field characteristics beyond degree 5, the field models are truncated to degree 5. Instead of applying lower bounds to data errors (which implies penalizing data of good quality), modelling errors due to the lower degree truncation are introduced in the data errors. Following a philosophy of using all information provided by the data, the

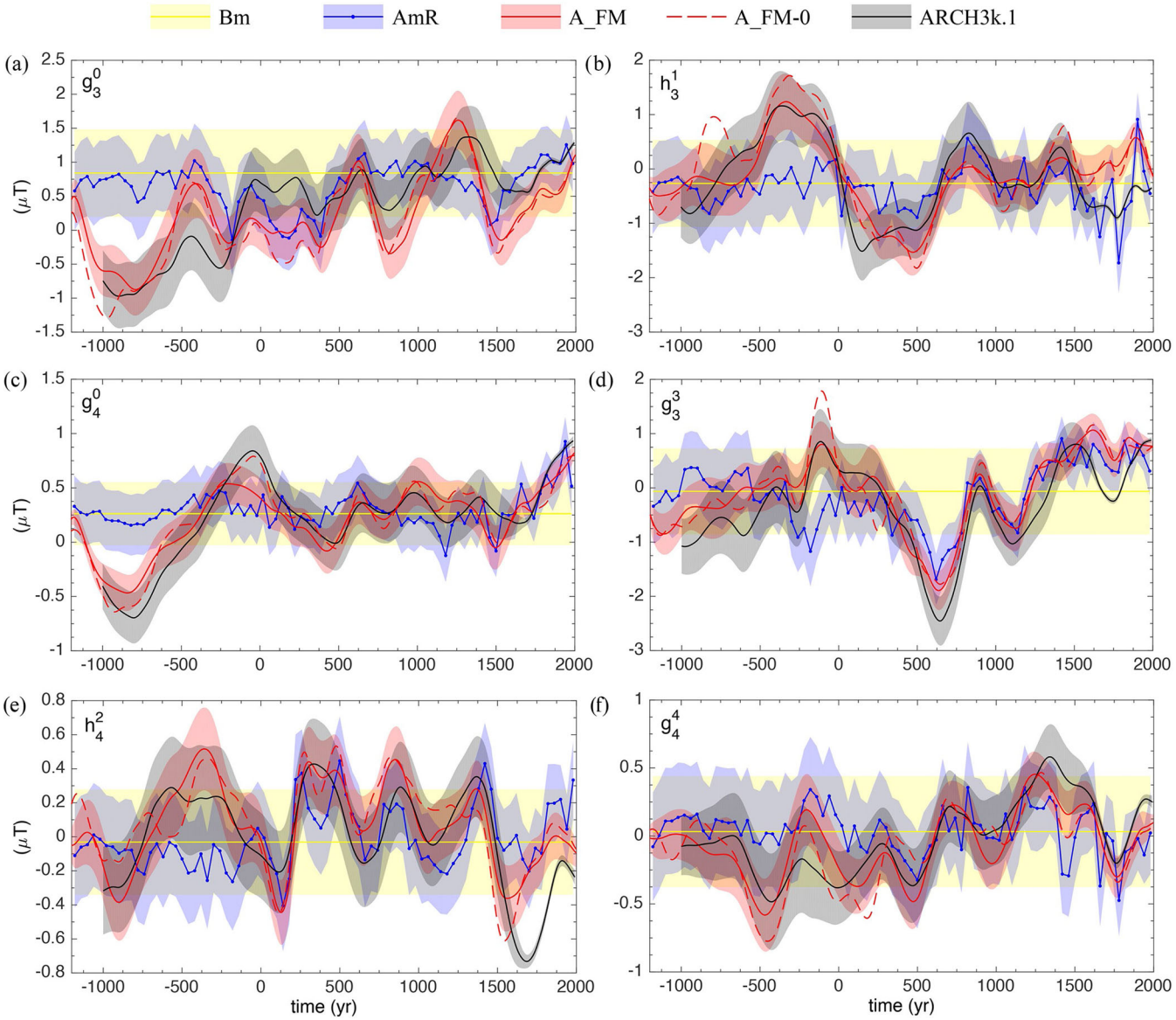

Figure 10. Continuation of Fig. 9 for higher order Gauss coefficients.

model applies an outlier re-weighting instead of a rejection scheme. While A_FM-0 is a direct inversion of the A_dat data set (restricted to volcanic and archaeological data), the A_FM model consists of an ensemble of models generated by a similar bootstrap technique as in Korte *et al.* (2009).

AmR: The AmR model is the result of an inverse scheme regularized by a non-adjustable spatial dynamo norm provided by the CE dynamo, using the full truncation of the latter. With respect to ARCH3k.1 and A_FM, it considers a hybrid approach to the handling of lower bounds/modelling errors relative to the data uncertainties (see Subsection 3.1). The redistributed R data set, from which the model is derived, is described in Section 3.2.

The differences between ARCH3k.1, A_FM and AmR are illustrated in Fig. 9 for the dipole and quadrupole terms and Fig. 10 for coefficients of degree 3 and above. AmR exhibits frequencies higher than those displayed by ARCH3k.1, A_FM, and A_FM-0, pointing to a weaker effective temporal regularization. As can be seen in Fig. 9(a), the four models concur on the intensity decrease of the axial dipole g_1^0 over the past millennium. The axial dipole shows a considerable decrease in the standard deviation from the background model Bm to the posterior model AmR, which could be expected from the archaeomagnetic resolution matrix (recall the first line in Fig. 6b). The general agreement of all models for g_1^0 reflects its control by the data set. Such a statement can also be made for the equatorial dipole coefficients, g_1^1 and h_1^1 in Figs 9(b) and (c). The uncertainty levels of the (g_1^0, g_1^1, h_1^1) triplet of the AmR model are in line with those predicted by A_FM and ARCH3k.1, except over 1600 AD–2000 AD when the latter is constrained by *gufm1*. Again, this agreement highlights the robust characterization of model uncertainties, strongly controlled by the characteristics of the common data set. The quadrupole coefficients (shown in Figs 9d–h) present more variability between models, in particular during the first millennium BC. In this case, the disagreement underlines the larger influence of the prior information supplied to the inversion scheme.

Higher order coefficients are exhibited in Fig. 10. They essentially show that before 0 AD, AmR is not properly updated from the background model Bm, both in terms of its mean value and

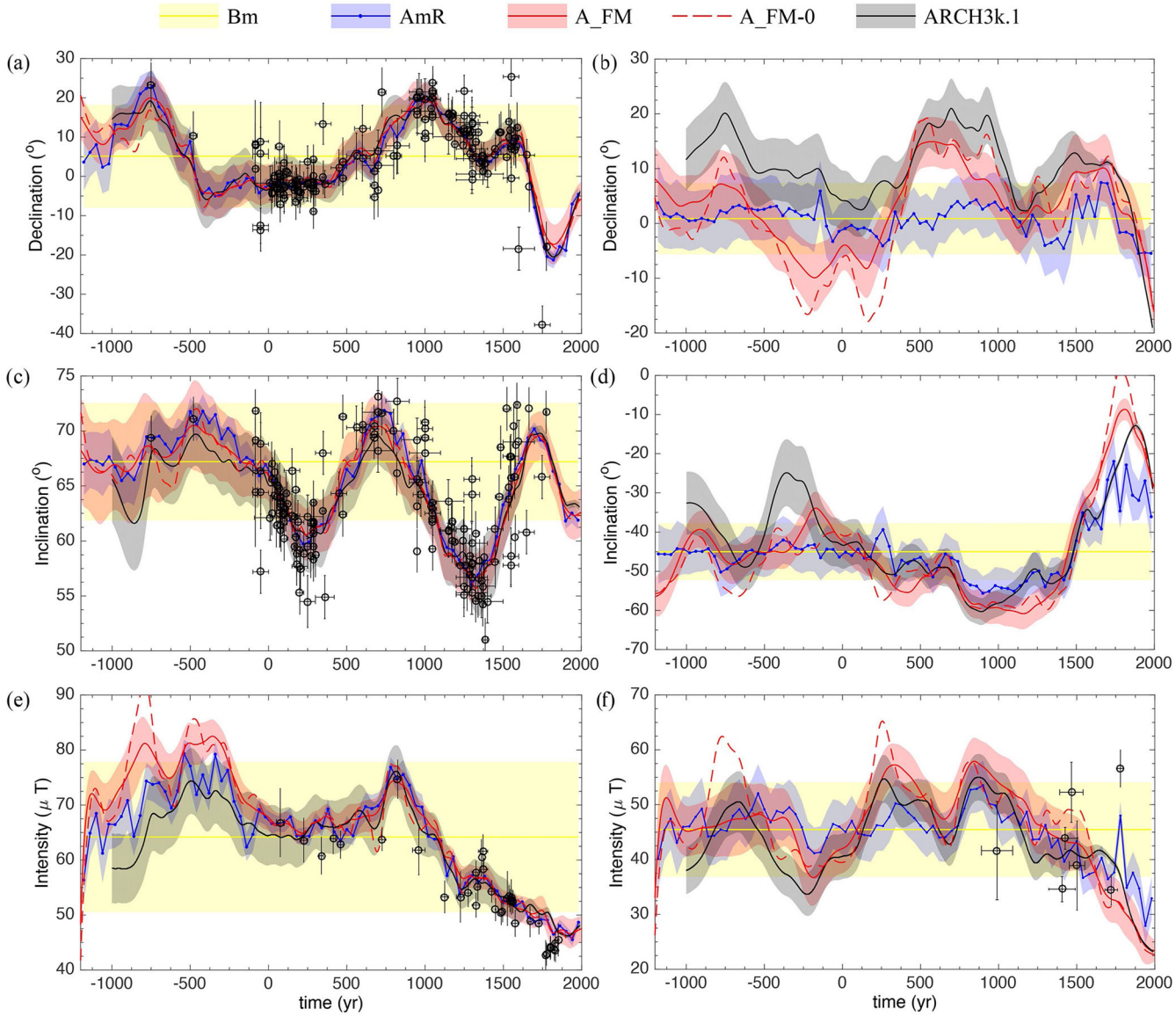

Figure 11. Projection of the ARCH3k.1 (black line with grey shadings), A_FM-M (red line with shadings), AFM-0 (red dashed line), AmR (blue line with shading) and Bm (yellow line with shading) models in Paris and São Paulo, and comparison with the available archaeomagnetic data. (a) Declination, (c) inclination and (e) intensity at Paris (location 48.85°N 2.35°E) for which data were collected over a disk of radius 300 km centred on Paris. (b) Declination, (d) inclination and (f) intensity at São Paulo (location 23.54°S 46.63°W) for which data were collected over a disk of radius 300 km centred on São Paulo.

respective uncertainty level. This indicates a poor sensitivity of the model to the data; see for instance the zonal coefficient g_4^0 in Fig. 10(c). Here, as in many other instances in Fig. 10, the estimate is strongly driven by the CE dynamo model. Periods of model-driven versus data-driven coefficient estimates are easy to assess, and they follow the information conveyed by the archaeomagnetic resolution matrix (recall Fig. 6b). In contrast, such distinction is less straightforward to make for ARCH3k.1 and A_FM. For instance, they do not show any significant increase of uncertainty estimates at times of paucity of data (see for instance the first 1000 yr of g_4^0 in Fig. 10c). Since these models prioritize fitting the data, they are prone to displaying a variability relatively higher than that of our estimate, which on the contrary favours geomagnetic quiescence (within the background uncertainty) at periods poorly documented by observations.

In order to further discuss the accuracy of the models in light of the available data, we show in Fig. 11 model predictions at Paris and São Paulo. In Fig. 11, left column, we report the direction and intensity data lying inside a circular region of 300 km radius around Paris. All models display a rather good agreement with the data, and a similar behaviour after 0 AD. The most significant difference among models is observed for intensity during the first millennium BC. This reflects a period poorly constrained by data, which puts consequently more weight to the prior chosen to construct any given model. Posterior model uncertainties vary considerably among models, regardless of the epoch. As stressed above, this is a consequence of different strategies to handle posterior model uncertainties: while the error on AmR is estimated from the standard deviation of the ensemble spread, ARCH3k.1 provides the error by propagating the coefficient uncertainties, and A_FM directly adds modelling errors to the ensemble standard deviation.

A different situation is found in Fig. 11, right column, where we show the model projections at São Paulo. Each model provides different evolutions, clearly in relation with the lack of data

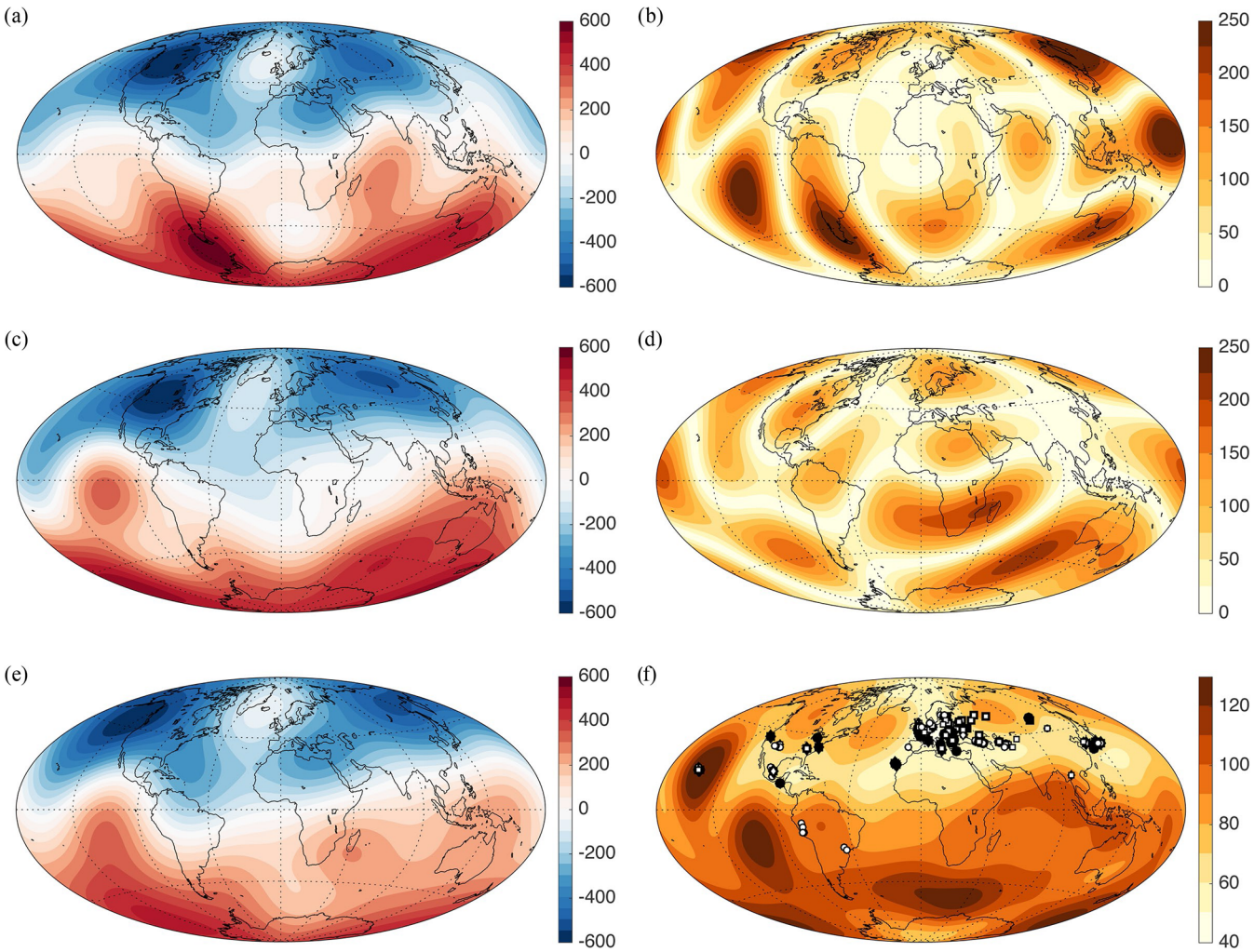

Figure 12. Different models of the magnetic field at the CMB for the time interval between 1680 AD and 1719 AD and its differences and uncertainties. (a), (c) and (e) show the average field for the 40-yr interval from the inverse models ARCH3k.1, AFM-M and our AmR model, respectively, with contours every 50 μT; (b) shows the absolute difference ||ARCH3k.1−AmR|| while (d) shows the absolute difference ||AFM-M−AmR||, with contours every 25 μT; (f) the standard deviation associated with the ensemble spread of AmR, with contours every 10 μT, overlapped by the R data set showing redistributed data, with high uncertainties, (in white) and non-redistributed data, with small uncertainties (in black). All values in μT.

in the Southern hemisphere. This is particularly evident for the declination: both ARCH3k.1 and A_FM give large amplitude fluctuations on centennial to millennial time scales, while AmR predictions favour geomagnetic quiescence, namely weak fluctuations around the background state, within the prior uncertainties. This contrasting behaviour must arise from the regional propagation of information by means of the prior correlations previously discussed in Section 2.5 and shown in Fig. 2. The impact of the spatial correlations arising from both the dynamo and the dissipation norms should be analysed with care. For instance, although the core field is indeed thought to display a certain degree of equatorial antisymmetry, the extent of it is unknown. In the archaeomagnetic case, in which observations are mostly located over the North Hemisphere, an excess in antisymmetric correlations could imply the masking of reversed flux patches over the South Hemisphere like the ones observed in the contemporary magnetic field (Jackson *et al.* 2000). However, this problem is a common drawback of archaeomagnetic inverse modelling and it can only be mitigated in light of new data.

Finally, a comparison of the radial induction B_r mapped at the CMB averaged over a time window of width 40 yr centred on 1700 AD between A_FM, ARCH3k.1 and AmR is shown in Fig. 12. We use that specific time interval in order to compare the situation in which one of the models, ARCH3k.1 (Fig. 12a), is partially regularized by *gufm1*, while A_FM and AmR are built exclusively with archaeomagnetic data. The three models show northern high latitude flux lobes underneath North America and Asia. Yet, the intensity and the location of the lobes predicted by AmR differ from those given by the other two models. In particular, the eastward offset of the American flux lobe in AmR might be interpreted as the influence of an eastward pull by the prior (see Fig. 1a), for which an intense flux patch is localized underneath North-East Asia. While the intensity of AmR seems reduced in comparison with the others, the general morphology of the field remains the same in all models. Still, the main differences between A_FM and ARCH3k.1 on the one hand, and AmR on the other hand occur mostly in the Southern hemisphere, as shown in Figs 12(b) and (d). Differences with ARCH3k.1 are more pronounced around Southernmost America and the South Pacific (but also on the Northernmost and central west Pacific), while the largest differences with A_FM occur in South Africa and the southern Indian ocean. The magnitude of these regional discordances are within the characteristic

posterior uncertainties of the AmR model, whose standard deviation is mapped in Fig. 12(f).

5 SUMMARY AND PERSPECTIVES

The main objective of this study is to present a framework for modelling the archaeomagnetic field at single epochs in which a set of directional and intensity data is complemented by the prior information from a geodynamo simulation. Here, the background information is represented by the mean and covariance of an ensemble of magnetic field states extracted from the long integration of a dynamo model, in this instance the CE model (Aubert *et al.* 2013). These statistics are used to define a spatial norm that enters the inverse archaeomagnetic problem. The dynamo norm considered in this work contrasts with the regularization norm based on minimum Ohmic used in standard inverse archaeomagnetic models. As shown in Figs 2(d) and (f), the dynamo norm places strong antisymmetrical constraints on the sought solution, as a consequence of the dominant axial dipolarity of the geodynamo. On the contrary, standard regularization norms lead to the spatial correlations implied by a dipole whose axis passes through the observation site. Once the simulation outputs are rescaled, the physics-based dynamo norm needs no further adjustment of the trade-off between goodness-of-fit and model complexity.

One of the most important aspects of using a dynamo norm in the single-epoch inverse archaeomagnetic problem is that it enables a straightforward computation of the resolution matrix associated with archaeomagnetic data. In this study, we use the Geomagia50.V2 database (Donadini *et al.* 2009) to ease comparison with previously published archaeomagnetic field models. Since these field models are constructed using some form of temporal regularization, we perform a redistribution of the archaeomagnetic data set in a discretized time interval from 1200 BC to 2000 AD, based on age uncertainties, thereby creating the R data set. The resulting archaeomagnetic resolution matrix, shown in Fig. 6, allows us to distinguish, for each coefficient, data-driven from prior-driven periods. The dipole, quadrupole, and to some extent the octupole, appear well resolved over the whole period. From 0 AD to 2000 AD, the degree 4 is resolved as well, whereas from 1000 AD onward, resolution is achieved up to degree 5. In both cases, an enhanced resolution is observed for sectoral coefficients. Beyond degree 5, the archaeomagnetic data set has almost no influence on coefficient estimates.

It is important to note that there has been new updates to the archaeomagnetic database used in this work, composing the Geomagia50.V3 database (Brown *et al.* 2015). We have performed exploratory tests within the new database, which incorporates valuable data on the Southern Hemisphere. Although we observe a slight increase in the overall resolution, the conclusions stated above based on the older database still hold. Despite the small improvement, we would like to acknowledge that this gain is incremental, and efforts in expanding the archaeomagnetic database are key to increasing the resolution of the core magnetic field through the past millennia.

We choose the R data set to build up a preliminary model, referred to as AmR. Comparison of Gauss coefficients predicted by AmR and ARCH3k.1 (Korte *et al.* 2009), AFM and AFM-0 (Licht *et al.* 2013) is in line with what is to be expected from the archaeomagnetic resolution matrix, despite the presence of outliers in the data set. In general, when coefficients are resolvable from the data, similar estimates are obtained, regardless of the model and methodology. Most differences are observed for those coefficients which are prior-driven. In the same way, pointwise predictions are in rough agreement in those regions where data are abundant, whereas stark differences are found in poorly documented areas.

In this study, attention was drawn to a sequence of independent snapshot analyses of the magnetic field through the last 3000 yr, assuming a constant background state. The next step will be to consider the temporal aspect of this scheme, and therefore the estimation of the state via a sequence of analysis cycles. More specifically, in a data assimilation framework such as the EnKF, an ensemble of states will be forecasted using the underlying numerical model, and this ensemble of forecasts will be used in conjunction with data (whenever they are available) to produce an ensemble of analyses, whose mean will hopefully be closer to the true state of Earth's core. In parallel, this novel approach will be strengthened by our ability to mitigate the impact of the strongly heterogeneous properties of the catalogue of data at our disposal.

ACKNOWLEDGEMENTS

We would like to thank F. Javier Pavón-Carrasco and an anonymous referee for the helpful and constructive reviews. We are also grateful to Sacha Brun, Andy Jackson and Erwan Thébault for fruitful exchanges and to Olivier Sirol for his assistance in the design of the calculations. This work has been supported by the French 'Agence Nationale de la Recherche' under the grant ANR-11-BS56-011. Numerical computations were performed at S-CAPAD, IPGP, France and using HPC resources from GENCI-IDRIS (Grants 2014-042122 and 2015-042122). This is IPGP contribution 3778.

REFERENCES

Alboussière, T., Deguen, R. & Melzani, M., 2010. Melting-induced stratification above the Earth's inner core due to convective translation, *Nature,* **466**(7307), 744–747.

Aubert, J., 2014. Earth's core internal dynamics 1840–2010 imaged by inverse geodynamo modelling, *Geophys. J. Int.,* **197**(3), 1321–1334.

Aubert, J. & Fournier, A., 2011. Inferring internal properties of Earth's core dynamics and their evolution from surface observations and a numerical geodynamo model, *Nonlinear Process. Geophys.,* **18**(5), 657–674.

Aubert, J., Finlay, C.C. & Fournier, A., 2013. Bottom-up control of geomagnetic secular variation by the Earth's inner core, *Nature,* **502**(7470), 219–223.

Bloxham, J. & Jackson, A., 1992. Time-dependent mapping of the magnetic field at the core-mantle boundary, *J. geophys. Res.,* **97**(B13), 19 537–19 563.

Bloxham, J., Gubbins, D. & Jackson, A., 1989. Geomagnetic secular variation, *Phil. Trans. R. Soc. Lond., A,* **329,** 415–502.

Braginsky, S.I. & Roberts, P.H., 1995. Equations governing convection in Earth's core and the geodynamo, *Geophys. Astrophys. Fluid Dyn.,* **79**(1), 1–97.

Brown, M.C., Donadini, F., Korte, M., Nilsson, A., Korhonen, K., Lodge, A., Lengyel, S.N. & Constable, C.G., 2015. Geomagia50.v3: 1. General structure and modifications to the archeological and volcanic database, *Earth Planets Space,* **67**(1), 1–31.

Burgers, G., van Leeuwen, P.J. & Evensen, G., 1998. Analysis scheme in the ensemble Kalman filter, *Mon. Weather Rev.,* **126**(6), 1719–1724.

Christensen, U. & Wicht, J., 2015. 8.10 - numerical dynamo simulations, in *Treatise on Geophysics,* 2nd edn, pp. 245–277, ed. Schubert, G., Elsevier.

Christensen, U.R., Aubert, J. & Hulot, G., 2010. Conditions for Earth-like geodynamo models, *Earth planet. Sci. Lett.,* **296**(3), 487–496.

Constable, C.G., Parker, R.L. & Stark, P.B., 1993. Geomagnetic field models incorporating frozen-flux constraints, *Geophys. J. Int.,* **113**(2), 419–433.

Donadini, F., Korhonen, K., Riisager, P. & Pesonen, L.J., 2006. Database for Holocene geomagnetic intensity information, *EOS, Trans. Am. geophys. Un.,* **87**(14), 137–143.

Donadini, F., Korte, M. & Constable, C., 2009. Geomagnetic field for 0–3 ka: 1. New data sets for global modeling, *Geochem. Geophys. Geosyst.,* **10**(6), doi:10.1029/2008GC002295.

Dormy, E., 1997. Modélisation numérique de la dynamo terrestre, *PhD thesis,* Institut de Physique du Globe de Paris.

Dumberry, M. & Finlay, C.C., 2007. Eastward and westward drift of the Earth's magnetic field for the last three millennia, *Earth planet. Sci. Lett.,* **254**(1), 146–157.

Evensen, G., 2003. The ensemble Kalman filter: theoretical formulation and practical implementation, *Ocean Dyn.,* **53**(4), 343–367.

Finlay, C.C. & Jackson, A., 2003. Equatorially dominated magnetic field change at the surface of Earth's core, *Science,* **300**(5628), 2084–2086.

Finlay, C.C. *et al.*, 2010. International geomagnetic reference field: the eleventh generation, *Geophys. J. Int.,* **183**(3), 1216–1230.

Finlay, C.C., 2012. Core processes: Earth's eccentric magnetic field, *Nat. Geosci.,* **5**(8), 523–524.

Fournier, A. *et al.*, 2010. An introduction to data assimilation and predictability in geomagnetism, *Space Sci. Rev.,* **155**(1–4), 247–291.

Fournier, A., Aubert, J. & Thébault, E., 2011. Inference on core surface flow from observations and 3-D dynamo modelling, *Geophys. J. Int.,* **186**(1), 118–136.

Fournier, A., Nerger, L. & Aubert, J., 2013. An ensemble Kalman filter for the time-dependent analysis of the geomagnetic field, *Geochem. Geophys. Geosyst.,* **14**(10), 4035–4043.

Genevey, A., Gallet, Y., Constable, C., Korte, M. & Hulot, G., 2008. Archeoint: an upgraded compilation of geomagnetic field intensity data for the past ten millennia and its application to the recovery of the past dipole moment, *Geochem. Geophys. Geosyst.,* **9**(4), doi:10.1029/2007GC001881.

Glatzmaier, G.A., 2002. Geodynamo simulations-how realistic are they?, *Annu. Rev. Earth Planet. Sci.,* **30**(1), 237–257.

Gubbins, D., 1975. Can the Earth's magnetic field be sustained by core oscillations?, *Geophys. Res. Lett.,* **2**(9), 409–412.

Gubbins, D. & Bloxham, J., 1985. Geomagnetic field analysis—III. Magnetic fields on the core-mantle boundary, *Geophys. J. Int.,* **80**(3), 695–713.

Gubbins, D. & Roberts, N., 1983. Use of the frozen flux approximation in the interpretation of archaeomagnetic and palaeomagnetic data, *Geophys. J. Int.,* **73**(3), 675–687.

Hartmann, G.A. & Pacca, I.G., 2009. Time evolution of the South Atlantic magnetic anomaly, *An. Acad. Bras. Cienc.,* **81**(2), 243–255.

Hellio, G., Gillet, N., Bouligand, C. & Jault, D., 2014. Stochastic modelling of regional archaeomagnetic series, *Geophys. J. Int.,* **199**(2), 931–943.

Hjorungnes, A. & Gesbert, D., 2007. Complex-valued matrix differentiation: techniques and key results, *IEEE Trans. Signal Process.,* **55**(6), 2740–2746.

Hongre, L., Hulot, G. & Khokhlov, A., 1998. An analysis of the geomagnetic field over the past 2000 years, *Phys. Earth planet. Inter.,* **106**(3), 311–335.

Jackson, A., Jonkers, A.R. & Walker, M.R., 2000. Four centuries of geomagnetic secular variation from historical records, *Phil. Trans. R. Soc. Lond., A,* **358**(1768), 957–990.

Jazwinski, A.H., 1970. *Stochastic Processes and Filtering Theory,* Academic Press.

Johnson, C.L. & Constable, C.G., 1997. The time-averaged geomagnetic field: global and regional biases for 0–5 Ma, *Geophys. J. Int.,* **131**(3), 643–666.

Kalnay, E., 2003. *Atmospheric Modeling, Data Assimilation, and Predictability,* Cambridge Univ. Press.

Korte, M. & Constable, C., 2005. The geomagnetic dipole moment over the last 7000 years–new results from a global model, *Earth planet. Sci. Lett.,* **236**(1), 348–358.

Korte, M. & Constable, C., 2008. Spatial and temporal resolution of millennial scale geomagnetic field models, *Adv. Space Res.,* **41**(1), 57–69.

Korte, M. & Constable, C., 2011. Improving geomagnetic field reconstructions for 0–3 ka, *Phys. Earth planet. Inter.,* **188**(3), 247–259.

Korte, M., Donadini, F. & Constable, C., 2009. Geomagnetic field for 0–3 ka: 2. A new series of time-varying global models, *Geochem. Geophys. Geosyst.,* **10**(6), doi:10.1029/2008GC002297.

Korte, M., Constable, C., Donadini, F. & Holme, R., 2011. Reconstructing the Holocene geomagnetic field, *Earth planet. Sci. Lett.,* **312**(3), 497–505.

Kuang, W., Tangborn, A., Wei, Z. & Sabaka, T., 2009. Constraining a numerical geodynamo model with 100 years of surface observations, *Geophys. J. Int.,* **179**(3), 1458–1468.

Lanos, P., 2004. Bayesian inference of calibration curves: application to archaeomagnetism, in *Tools for Constructing Chronologies,* pp. 43–82, ed. Buck, C.E. & Millard, A.R., Springer.

Lhuillier, F., Fournier, A., Hulot, G. & Aubert, J., 2011. The geomagnetic secular-variation timescale in observations and numerical dynamo models, *Geophys. Res. Lett.,* **38**(9), doi:10.1029/2011GL047356.

Li, K., Jackson, A. & Livermore, P.W., 2014. Variational data assimilation for a forced, inertia-free magnetohydrodynamic dynamo model, *Geophys. J. Int.,* **199**(3), 1662–1676.

Licht, A., Hulot, G., Gallet, Y. & Thébault, E., 2013. Ensembles of low degree archeomagnetic field models for the past three millennia, *Phys. Earth planet. Inter.,* **224,** 38–67.

Monnereau, M., Calvet, M., Margerin, L. & Souriau, A., 2010. Lopsided growth of Earth's inner core, *Science,* **328**(5981), 1014–1017.

Nilsson, A., Holme, R., Korte, M., Suttie, N. & Hill, M., 2014. Reconstructing Holocene geomagnetic field variation: new methods, models and implications, *Geophys. J. Int.,* **198**(1), 229–248.

Olson, P. & Deguen, R., 2012. Eccentricity of the geomagnetic dipole caused by lopsided inner core growth, *Nat. Geosci.,* **5**(8), 565–569.

Pavón-Carrasco, F.J., Osete, M.L., Torta, J.M. & De Santis, A., 2014. A geomagnetic field model for the Holocene based on archaeomagnetic and lava flow data, *Earth planet. Sci. Lett.,* **388,** 98–109.

Ramsey, C.B., 2009. Bayesian analysis of radiocarbon dates, *Radiocarbon,* **51**(1), 337–360.

Souriau, A. & Calvet, M., 2015. The Earth's cores, in *Treatise on Geophysics,* 2nd edn, pp. 725–757, ed. Schubert, G., Elsevier.

Tangborn, A. & Kuang, W., 2015. Geodynamo model and error parameter estimation using geomagnetic data assimilation, *Geophys. J. Int.,* **200**(1), 664–675.

Tarantola, A. & Valette, B., 1982. Generalized nonlinear inverse problems solved using the least squares criterion, *Rev. Geophys.,* **20**(2), 219–232.

APPENDIX: LINEARIZED OBSERVATION OPERATORS FOR DIRECTIONAL AND INTENSITY DATA

Real functions of complex variables are not holomorphic, and their gradients cannot be consequently defined in standard complex analysis (Hjorungnes & Gesbert 2007). However, a real-valued function f of a complex variable z can be written in terms of z and its complex conjugate $z^\dagger$, in order to get rid of a possible imaginary part of f. If we take z and $z^\dagger$ to represent independent variables, the differential of a functional $f(z, z^\dagger)$ is given by the Wirtinger derivatives

$$\mathrm{d}f = \frac{\partial f}{\partial z}\mathrm{d}z + \frac{\partial f}{\partial z^\dagger}\mathrm{d}z^\dagger, \tag{A1}$$

where $\partial f/\partial z$ ($\partial f/\partial z^\dagger$) is the derivative of f with respect to a reference point for a fixed $z^\dagger$ (z).

Rewriting the expression for the declination in eq. (19), we have

$$D\left(\ldots, \mathcal{P}_\ell^m, \ldots, \mathcal{P}_\ell^{m\dagger}, \ldots\right) = \arctan\left[\frac{\sum_{\ell,m}\frac{1}{2r_c}\ell(\ell+1)\left(\mathcal{P}_\ell^m \mathcal{G}_{Y\ell}^{m\,\dagger} + \mathcal{P}_\ell^{m\dagger}\mathcal{G}_{Y\ell}^{\ m}\right)}{\sum_{\ell,m}\frac{1}{2r_c}\ell(\ell+1)\left(\mathcal{P}_\ell^m \mathcal{G}_{X\ell}^{m\,\dagger} + \mathcal{P}_\ell^{m\dagger}\mathcal{G}_{X\ell}^{\ m}\right)}\right], \tag{A2}$$

where $\sum_{\ell,m}$ is a simplified notation for the previous double summation over ℓ and m. Differentiating the previous equation with respect

to $\mathcal{P}_{\ell'}^{m'}$, around $\mathcal{P}_{\ell',0}^{m'}$, we have that

$$\frac{\partial D}{\partial \mathcal{P}_{\ell}^{m}} = \frac{1}{1+(Y_0/X_0)^2} \times \left[\sum_{\ell',m'} \frac{\ell'(\ell'+1)}{2r_c}\delta_{\ell\ell'}\delta_{mm'}\left(\mathcal{G}_{Y_{\ell'}^{m'}}^{\dagger} X_0 - \mathcal{G}_{X_{\ell'}^{m'}}^{\dagger} Y_0\right)\right]\frac{1}{X_0^2}, \tag{A3}$$

where δ is the Kronecker symbol and X_0, Y_0 and Z_0 are the magnetic vector components obtained from the reference state $\mathbf{x}_0 = \left[\ldots, \mathcal{P}_{\ell,0}^{m}, \ldots, \mathcal{P}_{\ell,0}^{m\,\dagger}, \ldots\right]^T$. Upon simplification, we see that

$$\frac{\partial D}{\partial \mathcal{P}_{\ell}^{m}} = \frac{1}{H_0^2}\frac{\ell(\ell+1)}{2r_c}\left(X_0\mathcal{G}_{Y_{\ell}^{m}}^{\dagger} - Y_0\mathcal{G}_{X_{\ell}^{m}}^{\dagger}\right), \tag{A4}$$

in which $H_0 = \sqrt{X_0^2 + Y_0^2}$. Differentiating now with respect to $\mathcal{P}_{\ell'}^{m'\dagger}$

$$\frac{\partial D}{\partial \mathcal{P}_{\ell}^{m\dagger}} = \frac{1}{H_0^2}\frac{\ell(\ell+1)}{2r_c}\left(X_0\mathcal{G}_{Y_{\ell}^{m}} - Y_0\mathcal{G}_{X_{\ell}^{m}}\right). \tag{A5}$$

The linearization of the nonlinear declination operator, $\mathcal{H}_D(\mathbf{x})$ around $\mathbf{x}_0$, following eq. (4), which we define formally as

$$\left.\frac{\partial \mathcal{H}_D}{\partial \mathbf{x}}\right|_{\mathbf{x}=\mathbf{x}_0} \equiv \mathbf{H}_{D,0},$$

can be written in terms of its Wirtinger derivatives as

$$\mathbf{H}_{D,0} = \frac{1}{2r_c H_0^2}\left[\ldots, \ell(\ell+1)\left(X_0\mathcal{G}_{Y_{\ell}^{m}}^{\dagger} - Y_0\mathcal{G}_{X_{\ell}^{m}}^{\dagger}\right), \ldots, \ell(\ell+1)\left(X_0\mathcal{G}_{Y_{\ell}^{m}} - Y_0\mathcal{G}_{X_{\ell}^{m}}\right), \ldots\right]. \tag{A6}$$

In the course of the iterative scheme (eq. 2), this operator is to be applied to a generic incremental state vector of the form

$$\mathrm{d}\mathbf{x} = \left[\ldots, \mathrm{d}\mathcal{P}_{\ell}^{m}, \ldots, \mathrm{d}\mathcal{P}_{\ell}^{m\dagger}, \ldots\right]^T.$$

Using the same reasoning, we find the following expressions for the linearized inclination and intensity operators, $\mathbf{H}_{I,0}$ and $\mathbf{H}_{F,0}$:

$$\mathbf{H}_{I,0} = \frac{1}{2r_c F_0^2}\left[\ldots, \ell(\ell+1)\left(H_0\mathcal{G}_{Z_{\ell}^{m}}^{\dagger} + \frac{Z_0}{H_0}(X_0\mathcal{G}_{X_{\ell}^{m}}^{\dagger} + Y_0\mathcal{G}_{Y_{\ell}^{m}}^{\dagger})\right), \ldots, \ell(\ell+1)\left(H_0\mathcal{G}_{Z_{\ell}^{m}} + \frac{Z_0}{H_0}(X_0\mathcal{G}_{X_{\ell}^{m}} + Y_0\mathcal{G}_{Y_{\ell}^{m}})\right), \ldots\right], \tag{A7}$$

$$\mathbf{H}_{F,0} = \frac{1}{2r_c F_0}\left[\ldots, \ell(\ell+1)\left(X_0\mathcal{G}_{X_{\ell}^{m}}^{\dagger} + Y_0\mathcal{G}_{Y_{\ell}^{m}}^{\dagger} + Z_0\mathcal{G}_{Z_{\ell}^{m}}^{\dagger}\right), \ldots, \ell(\ell+1)\left(X_0\mathcal{G}_{X_{\ell}^{m}} + Y_0\mathcal{G}_{Y_{\ell}^{m}} + Z_0\mathcal{G}_{Z_{\ell}^{m}}\right), \ldots\right]. \tag{A8}$$

It is important to note that the use of the extended state vector and the Wirtinger derivatives to cope with the real-to-complex transformations could be avoided by using the real SH expansion given by eqs (11) and (12). However, since our main objective is to introduce the formalism which considers the prior information from the CE numerical model, we have preferred to maintain the complex-valued variables of the simulation as the model state vector.